

Trinuclear $\{M^1\}CN\{M^2\}_2$ Complexes ($M^1 = Cr^{III}, Fe^{III}, Co^{III}$; $M^2 = Cu^{II}, Ni^{II}, Mn^{II}$). Are Single Molecule Magnets Predictable?Mihail Atanasov,^{†,‡} Christoph Busche,[‡] Peter Comba,^{*,‡} Fadi El Hallak,[§] Bodo Martin,[‡] Gopalan Rajaraman,[‡] Joris van Slageren,[§] and Hubert Wadepohl[‡]*Institute of General and Inorganic Chemistry, Bulgarian Academy of Sciences, Acad. Georgi Bontchev Str. Bl.11, 1113 Sofia, Bulgaria, Universität Heidelberg, Anorganisch-Chemisches Institut, Im Neuenheimer Feld 270, D-69120 Heidelberg, Germany, and 1. Physikalisches Institut, Universität Stuttgart, Pfaffenwaldring 57, 70550 Stuttgart, Germany*

Received March 28, 2008

The reaction of the hexacyanometalates $K_3[M^1(CN)_6]$ ($M^1 = Cr^{III}, Fe^{III}, Co^{III}$) with the bispidine complexes $[M^2(L^1)(X)]^{n+}$ and $[M^2(L^2)(X)]^{n+}$ ($M^2 = Mn^{II}, Ni^{II}, Cu^{II}$; $L^1 = 3\text{-methyl-9-oxo-2,4-di-(2-pyridyl)-7-(2-pyridylmethyl)-3,7-diazabicyclo[3.3.1]nonane-1,5-dicarboxylic acid dimethyl ester}$; $L^2 = 3\text{-methyl-9-oxo-7-(2-pyridylmethyl)-2,4-di-(2-quinolyl)-3,7-diazabicyclo[3.3.1]nonane-1,5-dicarboxylic acid dimethyl ester}$; $X = \text{anion or solvent}$) in water–methanol mixtures affords trinuclear complexes with *cis*- or *trans*-arrangement of the bispidine-capped divalent metal centers around the hexacyanometalate. X-ray structural analyses of five members of this family of complexes (*cis*- $Fe[CuL^2]_2$, *trans*- $Fe[CuL^1]_2$, *cis*- $Co[CuL^2]_2$, *trans*- $Cr[MnL^1]_2$, *trans*- $Fe[MnL^1]_2$) and the magnetic data of the entire series are reported. The magnetic data of the cyanide bridged, ferromagnetically coupled *cis*- and *trans*- $Fe[ML]_2$ compounds ($M = Ni^{II}, Cu^{II}$) with $S = 3/2$ (Cu^{II}) and $S = 5/2$ (Ni^{II}) ground states are analyzed with an extended Heisenberg Hamiltonian which accounts for anisotropy and zero-field splitting, and the data of the Cu^{II} systems, for which structures are available, are thoroughly analyzed in terms of an orbital-dependent Heisenberg Hamiltonian, in which both spin–orbit coupling and low-symmetry ligand fields are taken into account. It is shown that the absence of single-molecule magnetic behavior in all spin clusters reported here is due to a large angular distortion of the $[Fe(CN)_6]^{3-}$ center and the concomitant quenching of orbital angular momentum of the Fe^{III} (${}^2T_{2g}$) ground state.

Introduction

Much effort has been directed to the synthesis and characterization of paramagnetic spin clusters with high total spin ground states and large magnetic anisotropy (large and negative axial (D) and small off-axial (E) zero field splitting parameters) because of their potential application as single molecule magnets (SMMs).^{1,2} The negative axial anisotropy stabilizes the sublevels with the highest components of the spin ($\pm M_s$) with respect to the lower M_s sublevels, and this creates a bistability gap and an energy barrier U for the reversal of the magnetization M . Therefore, below the blocking temperature T_B , the thermal energy is insufficient

to overcome U at the time scale of the experiment and the spin can be trapped in one of two configurations. This is achieved by application of a large magnetic field (H_{dc}), which saturates M , and removal of the field is accompanied by a slow decay of M toward zero with a specific relaxation time τ . In the limit of a thermally activated decay of M , U is proportional to $S^2|D|$ or $(S^2 - 1/4)|D|$ for molecules with integer or noninteger spin values S , respectively. At very low temperature and dependent on the applied magnetic field, quantum tunneling of the magnetization may lead to faster relaxation rates than those obtained through the thermally activated pathway ($U_{eff} > U$).

The majority of SMMs are derived from oligonuclear complexes bridged by oxo- and carboxylato groups, and this includes the Mn_{12} SMM and its derivatives.^{3–7} Here, the relatively large value of U results from a large spin ($S =$

* To whom correspondence should be addressed. E-mail: peter.comba@aci.uni-heidelberg.de. Fax: (+49) 6221-546617.

[†] Bulgarian Academy of Sciences.

[‡] Universität Heidelberg.

[§] Universität Stuttgart.

(1) Kahn, O. *Molecular Magnetism*; Wiley&Sons Inc.: New York, 1993.

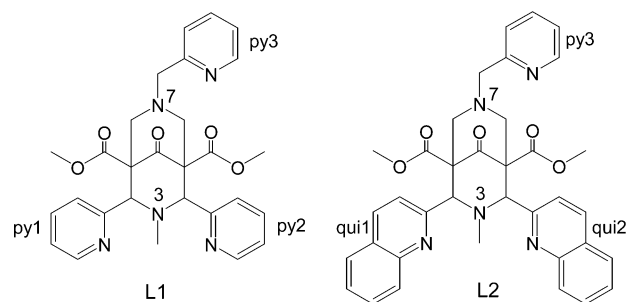
(2) Gatteschi, D. Sessoli, R.; Villain, J. *Molecular Nanomagnets*; Oxford University Press: Oxford, 2006.

(3) Lis, T. *Acta Crystallogr. B* **1980**, 36, 2042.

(4) Caneschi, A.; Gatteschi, D.; Sessoli, R.; Barra, A. L.; Brunel, L. C.; Guillot, M. *J. Am. Chem. Soc.* **1991**, 113, 5873.

10) but a moderate zero field splitting ($D \sim -0.5 \text{ cm}^{-1}$), which emerges from the values of D of the Jahn–Teller-elongated ($t_{2g}^3 e_g^1$) *high-spin* $\text{Mn}^{\text{III}}\text{O}_6$ centers. A different strategy applies to cyanometalate-based SMMs, analogues of the Prussian-blue-based high-temperature magnets,^{8,9} where relatively large values of D allow the use of moderate-sized complexes with relatively small values of the total spin S . The expected large negative value of the axial zero field splitting in these examples is the result of a large anisotropy of the $\text{M}^1\text{—CN—M}^2$ metal–ligand bonds with M^1 centers such as *low-spin* Fe^{III} or Mn^{III} with $^2\text{T}_{2g}(\text{O}_h)$ or $^3\text{T}_{1g}(\text{O}_h)$ ground states in the strong ligand field of cyanide. It has been shown that the unquenched momenta in these ground states and their mixing with the spin via first order spin–orbit coupling induce a strong anisotropy in $\text{Fe}^{\text{III}}\text{—CN—Cu}^{\text{II}}$ and $\text{Fe}^{\text{III}}\text{—CN—Ni}^{\text{II}}$ model complexes.^{10,11} When combined in an oligonuclear cyanometalate, these dinuclear units may, depending on the geometry, induce very large D values.¹¹ Various *low-spin* Fe^{III} cyanometalate spin clusters, based on a building-block synthetic strategy, where discrete molecular precursors are allowed to self-assemble to a common structural archetype, have been reported.^{12–32} With capping

Chart 1



ligands to prevent these units from growing toward one-, two-, or three-dimensional polymeric structures, impressive manifestations of the small S /large D effect on U have been reported. These include SMMs with linear trinuclear $[\text{M}^{\text{I}}\text{M}^{\text{II}}\text{M}^{\text{III}}]$ units ($\text{M} = \text{Fe}$: ferromagnetic coupling, $S = 9/2$ ground state; $\text{M} = \text{Cr}$: antiferromagnetic coupling, $S = 5/2$ ground state), with U_{eff} as large as 9.3 cm^{-1} and 16 cm^{-1} , respectively,^{25,33} and a trigonal bipyramidal $[\text{Cu}^{\text{II}}_3\text{Fe}^{\text{III}}_2]$ SMM with an $S = 5/2$ ground-state and $U_{\text{eff}} = 16 \text{ cm}^{-1}$.²⁰

As part of a continuing effort to prepare SMMs based on encapsulated cyanometalates,³⁴ and on the basis of our prediction of large anisotropies in dinuclear $\text{Fe}^{\text{III}}\text{—CN—M}^2$ subunits,¹¹ we now report the synthesis, structural characterization, and magnetic data of a family of trinuclear $\{[\text{M}^1(\text{CN})_6][\text{M}^2(\text{L})_2]\}$ complexes, where L is a pentadentate bispidine-type ligand (see Chart 1 for ligand structures, $\text{L}^1 = 3\text{-methyl-9-oxo-2,4-di-(2-pyridyl)-7-(2-pyridylmethyl)-3,7-diazabicyclo[3.3.1]nonane-1,5-dicarboxylic acid dimethyl ester}$; $\text{L}^2 = 3\text{-methyl-9-oxo-7-(2-pyridylmethyl)-2,4-di-(2-quinolyl)-3,7-diazabicyclo[3.3.1]nonane-1,5-dicarboxylic acid dimethyl ester}$), M^1 is Cr^{III} , Fe^{III} , or Co^{III} and M^2 is Mn^{II} , Ni^{II} , or Cu^{II} , and where the trinuclear complexes are linear (*trans*-configuration around M^1) or bent (*cis*-configuration around M^1).³⁵ The X-ray structural characterization of five members of this family is reported, the magnetic data of the four complexes with $\text{M}^1 = \text{Fe}^{\text{III}}$ and $\text{M}^2 = \text{Cu}^{\text{II}}$ or Ni^{II} are analyzed with an extended Heisenberg Hamiltonian which accounts for anisotropy and zero-field splitting, and the data of the systems with $\text{M}^2 = \text{Cu}^{\text{II}}$, for which structures are available, are thoroughly analyzed in terms of a recently developed extended orbital-dependent Heisenberg model.¹¹

- (5) Sessoli, R.; Tsai, H.-L.; Schake, A. R.; Wang, S.; Vincent, J. B.; Folting, K.; Gatteschi, D.; Christou, G.; Hendrickson, D. N. *J. Am. Chem. Soc.* **1993**, *115*, 1804.
- (6) Sessoli, R.; Gatteschi, D.; Caneschi, A.; Novak, M. A. *Nature* **1993**, *365*, 141.
- (7) Sessoli, R.; Gatteschi, D. *Angew. Chem., Int. Ed.* **2003**, *42*, 268.
- (8) Lescouëzec, R.; Toma, L. M.; Vaissermann, J.; Verdager, M.; Delgado, F. S.; Ruiz-Pérez, C.; Lloret, F.; Julve, M. *Coord. Chem. Rev.* **2005**, *249*, 2691.
- (9) Verdager, M.; Bleuzen, A.; Marvaud, V.; Vaissermann, J.; Seuleiman, M.; Desplanches, C.; Scullier, A.; Train, C.; Garde, R.; Gelly, G.; Lomench, C.; Rosenman, I.; Veillet, P.; Cartier, C.; Villain, F. *Coord. Chem. Rev.* **1999**, *192*, 1023.
- (10) Atanasov, M.; Comba, P.; Daul, C. A. *J. Phys. Chem. A* **2006**, *110*, 13332.
- (11) Atanasov, M.; Comba, P.; Daul, C. A. *Inorg. Chem.* **2008**, *47*, 2449.
- (12) Li, D.; Clérac, R.; Parkin, S.; Wang, G.; Yee, G. T.; Holmes, S. M. *Inorg. Chem.* **2006**, *45*, 5251.
- (13) Bartlett, B. M.; Harris, T. D.; DeGroot, M. W.; Long, J. R. *Z. Anorg. Allg. Chem.* **2007**, *633*, 2380.
- (14) Gu, Z.-G.; Yang, Q.-F.; Liu, W.; Song, Y.; Li, Y.-Z.; Zuo, J.-L.; You, X.-Z. *Inorg. Chem.* **2006**, *45*, 8895.
- (15) Li, D.; Parkin, S.; Wang, G.; Yee, G. T.; Clérac, R.; Wernsdorfer, W.; Holmes, S. M. *J. Am. Chem. Soc.* **2006**, *128*, 4214.
- (16) Oshio, H.; Tamada, O.; Onodera, H.; Ito, T.; Ikoma, T.; Tero-Kubota, S. *Inorg. Chem.* **1999**, *38*, 5686.
- (17) Oshio, H.; Yamamoto, M.; Ito, T. *Inorg. Chem.* **2002**, *41*, 5817.
- (18) Li, D.; Parkin, S.; Wang, G.; Yee, G. T.; Prosvirnin, A. V.; Holmes, S. M. *Inorg. Chem.* **2005**, *44*, 4903.
- (19) Liu, W.; Wang, C.-F.; Li, Y.-Z.; Zuo, J.-L.; You, X.-Z. *Inorg. Chem.* **2006**, *45*, 10058.
- (20) Wang, C.-F.; Zuo, J.-L.; Bartlett, B. M.; Song, Y.; Long, J. R.; You, X.-Z. *J. Am. Chem. Soc.* **2006**, *128*, 7162.
- (21) Gu, Z.-G.; Liu, W.; Yang, Q.-F.; Zhou, X.-H.; Zuo, J.-L.; You, X.-Z. *Inorg. Chem.* **2007**, *46*, 3236.
- (22) Van Langenberg, K.; Batten, S. R.; Berry, K. J.; Hockless, D. C. R.; Moubarak, B.; Murray, K. S. *Inorg. Chem.* **1997**, *36*, 5006.
- (23) Berlinguette, C. P.; Galán-Mascarós, J. R.; Dunbar, K. R. *Inorg. Chem.* **2003**, *42*, 3416.
- (24) Wang, S.; Zuo, J.-L.; Zhou, H.-C.; Choi, H. J.; Ke, Y.; Long, J. R.; You, X.-Z. *Angew. Chem., Int. Ed.* **2004**, *43*, 5940.
- (25) Choi, H. J.; Sokol, J. J.; Long, J. R. *Inorg. Chem.* **2004**, *43*, 1606.
- (26) Ni, W.-W.; Ni, Z.-H.; Cui, A.-L.; Liang, X.; Kou, H.-Z. *Inorg. Chem.* **2007**, *46*, 22.
- (27) Ni, Z.-H.; Kou, H.-Z.; Zhang, L.-F.; Ni, W.-W.; Jiang, Y.-B.; Cui, A.-L.; Ribas, J.; Sato, O. *Inorg. Chem.* **2005**, *44*, 9631.
- (28) Berlinguette, C. P.; Vaughn, D.; Cañada-Vilalta, C.; Galán-Mascarós, J. R.; Dunbar, K. R. *Angew. Chem.* **2003**, *115*, 1561.
- (29) Beltran, L. M. C.; Long, J. R. *Acc. Chem. Res.* **2005**, *38*, 325.

- (30) Rodríguez-Diéguez, A.; Kivekäs, R.; Sillanpää, R.; Cano, J.; Lloret, F.; McKee, V.; Stoeckli-Evans, H.; Colacio, E. *Inorg. Chem.* **2006**, *45*, 10537.
- (31) Toma, L. M.; Lescouëzec, R.; Pasán, J.; Ruiz-Pérez, C.; Vaissermann, J.; Cano, J.; Carrasco, R.; Wernsdorfer, W.; Lloret, F.; Julve, M. *J. Am. Chem. Soc.* **2006**, *128*, 4842.
- (32) Toma, L. M.; Delgado, F. S.; Ruiz-Pérez, C.; Carrasco, R.; Cano, J.; Lloret, F.; Julve, M. *J. Chem. Soc., Dalton Trans.* **2004**, 2836.
- (33) Ferbinteanu, M.; Miyasaka, H.; Wernsdorfer, W.; Nakata, K.; Sugiura, K.; Yamashita, M.; Coulon, C.; Clérac, R. *J. Am. Chem. Soc.* **2005**, *127*, 3090.
- (34) Atanasov, M.; Comba, P.; Lampeka, Y. D.; Linti, G.; Malcherek, T.; Miletich, R.; Prikhod'ko, A. I.; Pritzkow, H. *Chem.—Eur. J.* **2006**, *12*, 737.
- (35) The general nomenclature used in this manuscript, *cis*- and *trans*- $\text{M}^1[\text{M}^2\text{L}]_2$ does not include the bridging ligands (generally CN^-) and the charge of the trinuclear complexes (generally $+1$).

Results

Syntheses and Structural Properties of *cis*- and *trans*-M^I[M^{II}L]₂. The bispidine ligands were prepared as described before^{36–38} and general aspects of bispidine coordination chemistry have been reviewed;³⁹ reaction of L¹ and L² with salts of M² = Mn^{II}, Ni^{II}, or Cu^{II} produces the expected complexes in good yields (see Experimental Section). These M² fragments were reacted with the hexacyanometalates of M^I = Cr^{III}, Fe^{III}, and Co^{III} in H₂O/MeOH mixtures to produce the desired trinuclear, cyano-bridged *cis*- and *trans*-M^I[M^{II}L]₂ complexes in acceptable yields.

The packing of the large complex cations together with the small anions in the crystals is not very efficient and results in considerable voids in the structures which are occupied by the anions together with variable amounts of solvent (mostly water). In several cases, unambiguous assignment of the difference Fourier peaks within these voids to the anions (especially chloride) was not possible. We believe this to be due to the presence of several possible positions for the small anions in between the voluminous cations. As a consequence of electroneutrality, the anion sites become only partly occupied and quite difficult to differentiate from neutral solvent molecules (see also Experimental Section).

An interesting observation is that with L¹ the linear isomers (*trans*-configuration of the hexacyanometalate center) and with L² the bent isomers (*cis*-configuration of the central hexacyanometalate unit) are selectively formed (see Figure 1 and Table 1). This probably is due to a combination of weak intramolecular effects (van der Waals repulsion, π -stacking) and packing forces. All Cu^{II} subunits have an elongation along the ar1–Cu–ar2 axis (see Table 1). While for L², this was expected,³⁸ all Cu^{II} complexes of L¹ reported so far have an elongation along N7–Cu–py3.³⁹ It is, however, not unexpected that in the compounds studied here, there is a switch in the direction of the pseudo-Jahn–Teller elongation: bispidine-copper(II) complexes are known to have the three possible minimum structures at similar energies,^{40,41} and the cyanide ligand is known to induce a strong ligand field and therefore leads to a destabilization of the structure with an elongated CN–Cu–N7 axis. Consequently, the most stable structure has a Jahn–Teller-elongated ar1–Cu–ar2 axis and a strong bond to the cyanide bridge, and this is an important feature for the magnetic exchange mechanism.

We have not been able to crystallize the corresponding Ni^{II} complexes. However, from a combination of structural and thermodynamic data on bispidine complexes with a range

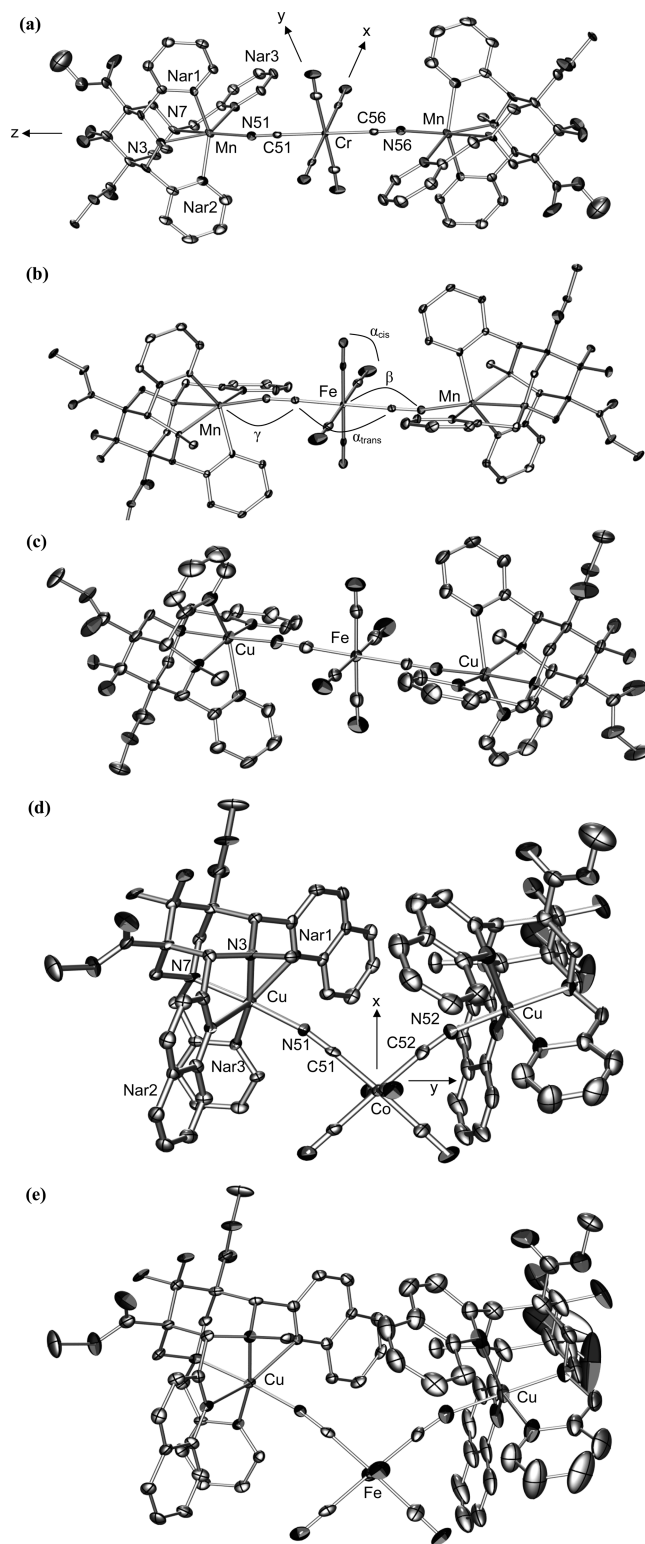


Figure 1. Plots of the molecular cations of the crystallographically analyzed trinuclear complexes. (a) *trans*-{Cr[MnL¹]₂}Cl, (b) *trans*-{Fe[MnL¹]₂}Cl, (c) *trans*-{Fe[CuL¹]₂}ClO₄, (d) *cis*-{Co[CuL²]₂}ClO₄, (e) *cis*-{Fe[CuL²]₂}ClO₄. Also shown are the atom numbering, the coordinate systems used for the analysis of the magnetic properties (also shown in Figure 11), and the definition of important structural parameters (see text).

of divalent transition metal ions it follows that the distortions observed for the Cu^{II} complexes are to a large extent enforced by the ligand backbone, that is, the structural features observed for Cu^{II} are not primarily due to the electronics of

- (36) Merz, K. W.; Haller, R. *Pharm. Acta Helv.* **1963**, 38, 442.
- (37) Börzel, H.; Comba, P.; Hagen, K. S.; Merz, M.; Lampeka, Y. D.; Lienke, A.; Linti, G.; Pritzkow, H.; Tsybal, L. V. *Inorg. Chim. Acta* **2002**, 337, 407.
- (38) Comba, P.; Lopez de Laorden, C.; Pritzkow, H. *Helv. Chim. Acta* **2005**, 88, 647.
- (39) Comba, P.; Kerscher, M.; Schiek, W. *Prog. Inorg. Chem.* **2007**, 55, 613.
- (40) Comba, P.; Hauser, A.; Kerscher, M.; Pritzkow, H. *Angew. Chem., Int. Ed.* **2003**, 42, 4536.
- (41) Bentz, A.; Comba, P.; Deeth, R. J.; Kerscher, M.; Pritzkow, H.; Seibold, B.; Wade, H. 2008; submitted for publication.

Table 1. Selected Structural Data of Three Linear and Two Bent $M^I[M^2L]_2$ Complexes^a

	<i>trans</i> -[(L ^I)Mn ^{II}] ₂ [Cr ^{III} (CN) ₆] ₂ Cl	<i>trans</i> -[(L ^I)Mn ^{II}] ₂ [Fe ^{III} (CN) ₆] ₂ Cl	<i>trans</i> -[(L ^I)Cu ^{II}] ₂ [Fe ^{III} (CN) ₆] ₂ ClO ₄	<i>cis</i> -[(L ²)Cu ^{II}] ₂ [Co ^{III} (CN) ₆] ₂ ClO ₄	<i>cis</i> -[(L ²)Cu ^{II}] ₂ [Fe ^{III} (CN) ₆] ₂ ClO ₄
Distances [Å]					
M ² –N(3)/M ² –N(3b)	2.274(3)/ <i>b</i>	2.279(2)/ <i>b</i>	2.111(3)/2.100(3)	2.077(3)/2.086(4)	2.080(7)/2.074(5)
M ² –N(7)/M ² –N(7b)	2.336(3)/ <i>b</i>	2.352(2)/ <i>b</i>	2.050(3)/2.056(3)	2.092(3)/2.055(4)	2.053(6)/2.085(5)
M ² –Nar ₁ /M ² –Nar _{1b}	2.242(3)/ <i>b</i>	2.249(2)/ <i>b</i>	---/2.346(3)	2.445(3)/2.360(4)	---/2.407(5)
M ² –Nar ₂ /M ² –Nar _{2b}	2.293(3)/ <i>b</i>	2.352(2)/ <i>b</i>	2.370(3)/---	2.407(3)/---	2.370(6)/2.440(5)
M ² –Nar ₃ /M ² –Nar _{3b}	2.231(3)/ <i>b</i>	2.228(2)/ <i>b</i>	2.045(3)/2.033(3)	2.077(3)/2.086(4)	2.022(7)/2.014(5)
M ² –N(NC)/M ² –N(NC)	2.145(4)/ <i>b</i>	2.136(2)/ <i>b</i>	1.964(3)/1.957(3)	1.996(3)/1.952(4)	1.938(6)/1.995(5)
M ² –M ¹ /M ² –M ¹	5.3294(7)/ <i>b</i>	5.1402(6)/ <i>b</i>	5.0025(12)/5.0164(12)	4.9853(8)/4.8937(9)	4.9358(12)/5.0286(11)
R	2.075 ± 0.003	1.937 ± 0.015	1.940 ± 0.014	1.896 ± 0.007	1.940 ± 0.016
Angles [deg]					
γ	167.7	161.8	171.0 ± 2.56	165.0	165.5 ± 2.12
β	176.57 ± 0.45	177.93 ± 0.76	178.48 ± 0.91	176.4 ± 2.06	176.42 ± 1.98
α _{cis}	88.16 ± 1.2	90.10 ± 2.66	90.00 ± 1.32	90.26 ± 2.34	89.99 ± 2.43
α _{trans}	<i>b</i>	<i>b</i>	178.69 ± 0.66	177.38 ± 0.77	177.1 ± 1.35

^a See Supplementary Information for the full structural data set. *R* is the average M¹–CN distance; γ is the average M²–N–C angle; β is the average M¹–C–N angle and α_{cis}, α_{trans} are the averages of the angles C–M¹–C (see Figure 1). ^b Dependent due to the inversion center on the central atom.

the metal center and therefore, to some extent at least, are also present in complexes with other electronic preferences, for example, Co^{II}, Ni^{II}, and Zn^{II}.^{39,42}

There are three geometric parameters which have a major influence on the magnetic coupling of the metal centers in cyanometalate-based oligonuclear complexes (see below): (i) the linearity of the cyanide bridge (β = M¹–C–N; γ = M²–N–C, see Table 1, see also Figure 1);⁴³ (ii) the geometry of the cyanometalate center (α_{cis}, α_{trans} = C–M¹–C, see Table 1, see also Figure 1); (iii) the tetragonal compression (elongation) of the cyanide-bridged terminal subunits (the M²–NC distances) and the corresponding M¹–CN distances *R* (see Table 1). The geometry of the terminal groups (M²–NC distances) can be enforced by the bispidine ligands to some extent (see above, see also Table 1). The M¹–CN distances are in the expected range and do not vary much with the geometries (linear vs bent) and end groups (M² = Mn^{II}, Cu^{II}, (Ni^{II})). The angular distortions (α, β, γ), which have a strong influence on the magnetic anisotropy (see below),¹¹ in particular the bending of the cyanide bridges (β, γ), are significant (see Table 1) and do not seem to follow a particular pattern. This is *the* major problem in designing cyanometalate-based SMMs (see also Discussion and Conclusion).

Magnetic Properties of *cis*- and *trans*-M^I[M²L]₂. The magnetization and χ*T* data of the whole series of trinuclear complexes are presented in Figure 2 and Table 2. For both *cis*- and *trans*-configurations a complex with a diamagnetic hexacyanometalate center was prepared and these *low-spin* [Co^{III}(CN)₆]³⁻ based complexes induce almost no coupling between the Cu^{II} centers. The coupling of the metal centers generally is ferromagnetic with the exception of *trans*-Cr[MnL]₂ which, because of the π-overlap between the unpaired electrons in t_{2g} orbitals of Cr^{III} (t_{2g}³) and Mn^{II} (t_{2g}³e_g²), shows an antiferromagnetic coupling behavior. For the *trans*-Fe[MnL]₂ complexes the χ*T* versus *T* data could only be simulated with a Heisenberg model with ferromag-

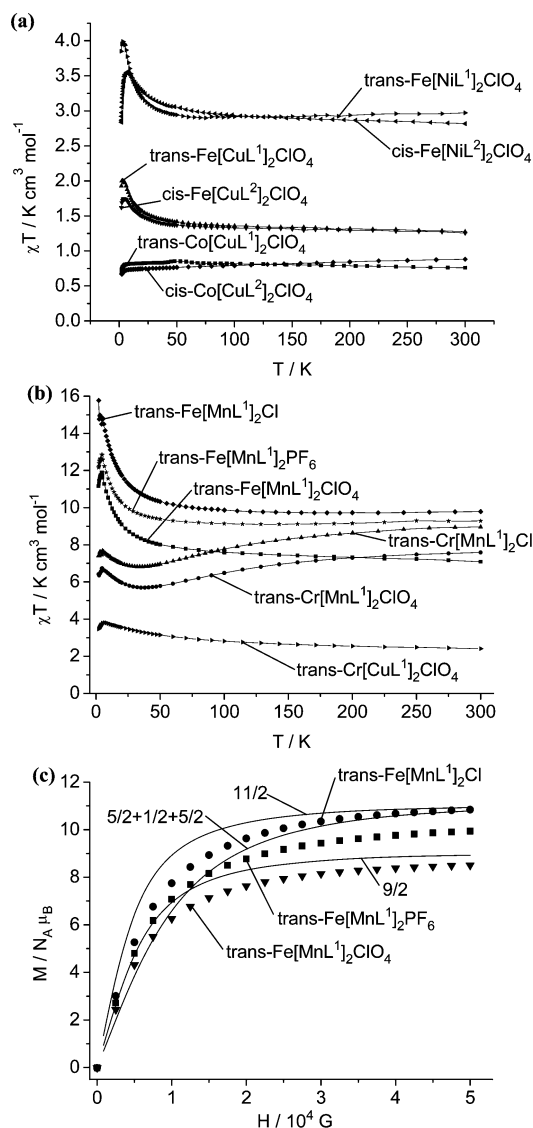


Figure 2. (a, b) Comparison of the χ*T* vs *T* plot of the M^I[M²L]₂ complexes. All samples were measured at an applied field of 0.1 T, except for the Ni^{II} complexes, which were measured at 0.05 T. (c) Magnetization (in units of *N_A* μ_B) of various salts of the *trans*-Fe[MnL]₂ complex, and Brillouin functions for ferromagnetic and antiferromagnetic coupling and uncoupled spins (2 K, *g* = 2).

(42) Born, K.; Comba, P.; Ferrari, R.; Kuwata, S.; Lawrance, G. A.; Wade, H. *Inorg. Chem.* **2007**, *46*, 458.

(43) Rodríguez-Fortea, A.; Alemany, P.; Alvarez, S.; Ruiz, E.; Sculler, A.; Decroix, C.; Marvaud, V.; Vaissermann, J.; Verdager, M.; Rosenman, I.; Julve, M. *Inorg. Chem.* **2001**, *40*, 5868.

Table 2. χT Values ($\text{cm}^3 \text{ K mol}^{-1}$; T [K] in brackets, $H = 1000 \text{ G}$) and High Field Magnetization (M [$N_A \mu_B$], $T = 1.8 \text{ K}$, $H = 50 \text{ kG}$)

complex	χT (exp)	χT (calc)	M (exp)	M (calc)
<i>cis</i> -Co[CuL ²] ₂ ClO ₄	0.882 (300.0) 0.670 (2.0)	0.750 ^b 0.750 ^b	1.71 ^c	2
<i>cis</i> -Fe[NiL ²] ₂ ClO ₄	2.817 ^a (300.0) 3.571 ^a (6.0)	2.375 ^b 4.377	4.42 ^d	5
<i>cis</i> -Fe[CuL ²] ₂ ClO ₄	1.254 (300.0) 1.748 (3.97)	1.125 ^b 1.876	2.60 ^d	3
<i>trans</i> -Co[CuL ¹] ₂ ClO ₄	0.759 (300.0) 0.705 (2.0)	0.750 ^b 0.750 ^b	1.99 ^c	2
<i>trans</i> -Fe[CuL ¹] ₂ ClO ₄	1.306 (300.0) 2.004 (2.87)	1.125 ^b 1.876	3.04 ^d	3
<i>trans</i> -Fe[NiL ¹] ₂ ClO ₄	2.970 ^a (300.0) 3.988 ^a (3.4)	2.375 ^b 4.377	4.68 ^d	5
<i>trans</i> -Fe[MnL ¹] ₂ ClO ₄	7.085 (300.0) 11.742 (3.52)	9.129 ^b 12.380	8.51 ^c	11
<i>trans</i> -Fe[MnL ¹] ₂ Cl	9.613 (300.0) 14.560 (3.77)	9.129 ^b 12.380	10.84 ^c	11
<i>trans</i> -Fe[MnL ¹] ₂ PF ₆	9.286 (300.0) 12.845 (4.52)	9.129 ^b 12.380	9.94	11
<i>trans</i> -Cr[MnL ¹] ₂ ClO ₄	7.595 (300.0) 6.734 (4.78)	10.630 ^b 7.878	5.70 ^c	7
<i>trans</i> -Cr[MnL ¹] ₂ Cl	8.958 ^a (300.0) 7.670 ^a (5.0)	10.630 ^b 7.878	6.87 ^c	7
<i>trans</i> -Cr[CuL ¹] ₂ ClO ₄	2.406 (300.0) 3.801 (6.49)	2.626 ^b 4.377	4.44 ^c	5

^a $H = 500 \text{ G}$. ^b Three uncoupled metal centers. ^c 2 K . ^d 70 kG .

Table 3. Exchange Coupling Constants from the Simulation of the Magnetic Susceptibility of *cis*- and *trans*-Fe[ML]₂ ($M = \text{Cu}^{\text{II}}$, Ni^{II})^a

complex	$J(\text{M}^{\text{II}}-\text{M}^{\text{III}})$		$J(\text{M}^{\text{II}}-\text{M}^{\text{II}})$	
	exp	DFT	exp	DFT
<i>trans</i> -Fe[CuL ¹] ₂ ClO ₄				
model 1	18.8	21.0	-6.6	2.2
model 2 $J(E)$	24.0	19.4	2.0	
model 2 $J(B_2)$	1.9	1.6		
<i>cis</i> -Fe[CuL ²] ₂ ClO ₄				
model 1	14.1	22.2	-6.1	
model 2 $J(E)$	25.4	19.4 ¹¹	2.3	
model 2 $J(B_2)$	1.6	1.6 ¹¹		
<i>trans</i> -Fe[NiL ¹] ₂ ClO ₄				
model 1	15.7		-4.0	
<i>cis</i> -Fe[NiL ²] ₂ ClO ₄				
model 1	11.4		-2.9	
<i>cis</i> -Co[CuL ²] ₂ ClO ₄				
model 1	0.0		-0.3	
<i>trans</i> -Co[CuL ¹] ₂ ClO ₄				
model 1	0.0		-0.5	
<i>trans</i> -Fe[MnL ¹] ₂ Cl				
model 1	8.0		-0.5	
<i>trans</i> -Fe[MnL ¹] ₂ PF ₆				
model 1	4.2		-0.2	
<i>trans</i> -Fe[MnL ¹] ₂ ClO ₄				
model 1	11.0		-0.6	
<i>trans</i> -Cr[MnL ¹] ₂ Cl				
model 1	-12.8		0.9	
<i>trans</i> -Cr[MnL ¹] ₂ ClO ₄				
model 1	-13.8		0.0	
<i>trans</i> -Cr[CuL ¹] ₂ ClO ₄				
model 1	5.1		-0.6	

^a Using an isotropic exchange coupling Hamiltonian $H_{\text{exc}} = -J(\text{M}^{\text{II}}-\text{M}^{\text{III}})(\mathbf{S}_1 \cdot \mathbf{S}_2 + \mathbf{S}_1 \cdot \mathbf{S}_3) - J(\text{M}^{\text{II}}-\text{M}^{\text{II}})\mathbf{S}_2 \cdot \mathbf{S}_3$ of model 1 and ignoring the low-temperature part; the parameters used in model 2 are also given for for *cis*- and *trans*-Fe[CuL]₂.

netic Fe–Mn exchange coupling. $\text{M}^{\text{III}}-\text{M}^{\text{II}}$ and $\text{M}^{\text{II}}-\text{M}^{\text{II}}$ exchange coupling energies from these simulations are listed in Table 3 (see Supporting Information for experimental and simulated χT vs T data). The field-dependent magnetization of the Cl^- salt of *trans*-Fe[MnL¹]₂ (Figure 2c, $T = 1.8 \text{ K}$) with $M = 10.84$ has a value of the magnetization as expected

for ferromagnetically coupled $\text{Fe}^{\text{III}}-\text{Mn}^{\text{II}}$ pairs ($M = 11$). This is shown in Figure 2c in comparison with calculations based on the Brillouin function and the assumption of ferromagnetic ($S = 11/2$) or antiferromagnetic ($S = 9/2$) coupling or uncoupled spins of the Mn^{II} and Fe^{III} sites ($S_{\text{Mn}^{\text{II}}} = 5/2$, $S_{\text{Fe}^{\text{III}}} = 1/2$). The saturated value of the magnetic moment is lower in the case of the PF_6^- salt of *trans*-Fe[MnL¹]₂ ($M = 9.94$) and even more so for the ClO_4^- salt ($M = 8.51$). We will show below that these effects can be attributed to the magnetic anisotropy emerging from the *low-spin*-[Fe(CN)₆]³⁻ subunit, which becomes particularly pronounced at low temperatures.

We will now focus on the *cis*- and *trans*-Fe[CuL]₂ and Fe[NiL]₂ complexes. The χT versus T data are simulated and their magnetic properties interpreted with three different exchange Hamiltonians, model 1, model 2, and model 3 (for details see also the paragraph “Theoretical Background” in the Experimental Section). Model 1 is based on a classical isotropic Heisenberg Hamiltonian with the two parameters J and J' describing the M^1-M^2 and the $\text{M}^2-\text{M}^{2'}$ couplings ($\text{M}^1 = \text{Fe}^{\text{III}}$, $\text{M}^2 = \text{Cu}^{\text{II}}$ or Ni^{II}), respectively. Model 2 is an extended and orbital-dependent Heisenberg model which also accounts for orbital degeneracy and spin–orbit coupling within the $^2\text{T}_{2g}$ ground-state manifold of $[\text{Fe}(\text{CN})_6]^{3-}$.¹¹ The approach involves a full CI within the basis of the 252 Slater determinants as well as low-symmetry ligand field distortions. The ligand field matrices are computed by single-point DFT calculations, based on the X-ray structural data. Model 3 is an extension of model 1 for systems with no structural data available, which accounts for the zero-field splitting of the ferromagnetic spin ground-state in terms of two parameters, D and E for axial and rhombic distortions, respectively.

Magnetic Properties of *cis*- and *trans*-Fe[CuL]₂ and Fe[NiL]₂. *trans*-Fe[CuL]₂. Magnetic susceptibility measurements were performed on powdered crystals of *trans*-Fe[CuL]₂ at 1000 G in the temperature range of 2–300 K. The room temperature χT value of $1.306 \text{ emu K mol}^{-1}$ is very close to that expected for three uncoupled $S = 1/2$ spins (spin-only value: $1.125 \text{ emu K mol}^{-1}$). The χT value increases to a maximum of $2.00 \text{ emu K mol}^{-1}$ at a temperature of 2.87 K, which is slightly higher than expected for an $S = 3/2$ ground state (spin-only 1.875), and clearly manifests a ferromagnetic Fe–Cu coupling (see Figure 3a). This is further supported by the field dependence of the magnetization (M at 1.8 K, Figure 3c), which shows the saturation expected for an $S = 3/2$ ground state. A reasonable fit of the χT versus T data was possible on the basis of isotropic exchange with model 1 (Figure 3a). The value of the Cu–Fe exchange coupling energy ($J = 18.8 \text{ cm}^{-1}$), deduced from the χT versus T simulation is close to literature values reported for other cyanide-bridged Cu–Fe complexes, based on the same model (e.g., in a $[\text{Cu}_3\text{Fe}_2]$ SMM, $J = 17.0 \text{ cm}^{-120}$), and also to the value deduced from DFT calculations ($J = 22.0 \text{ cm}^{-1}$, see Table 3). When model 1 is used, the Cu–Cu exchange coupling is found to be significant and antiferromagnetic. This is in contrast to the magnetic data for the isostructural *trans*-Co[CuL]₂ complex, which shows little or no Cu–Cu exchange coupling (see Table 3

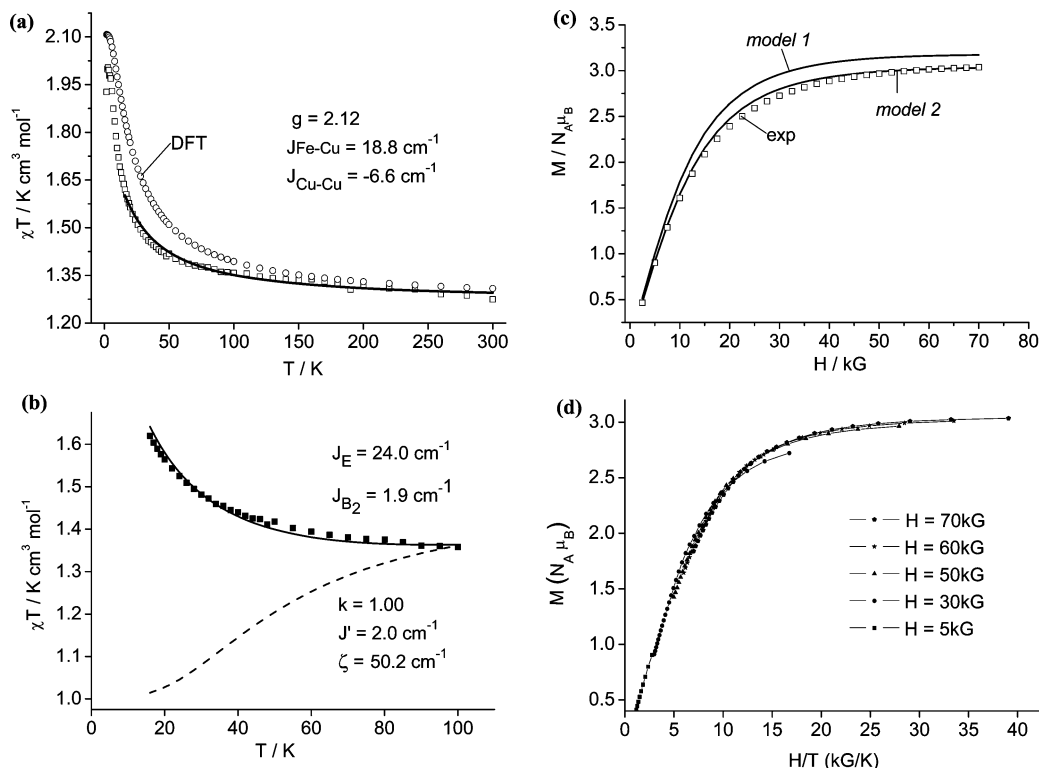


Figure 3. Magnetic properties of *trans*-Fe[CuL¹]₂, experimental data of the ClO₄ salt; (a) χT vs T diagram (open squares), the corresponding DFT-computed values (open circles), and the best fit (*model 1*, solid line) with $J(\text{Cu}-\text{Fe}) = 18.8$, $J(\text{Cu}-\text{Cu}) = -6.6$ and $g = 2.12$. (b) χT vs T experimental data (black squares), simulation using *model 2* [$g(\text{Cu}) = 2.15$] (black line), and calculation based on a regular octahedral $[\text{Fe}(\text{CN})_6]^{3-}$ site (dashed line); (c) magnetization M (in units of $N_A\mu_B$) vs magnetic field plot ($T = 1.8$ K); experimental data (open squares), and simulations (parameters as above) using *model 1* and *model 2* (solid lines); (d) field dependencies of the reduced magnetization (in units of $N_A\mu_B$; $T = 1.8$ K).

and Supporting Information), and the DFT calculations, which yield a small but positive value of J' (ferromagnetic coupling).

A possible reason for this discrepancy is that *model 1* completely ignores the Fe^{III} multiplet structure (orbital degeneracy) and spin–orbit coupling. The crystal and molecular structure of *trans*-Fe[CuL¹]₂ is of good quality (see above) and has therefore been used to compute the sublevels of the $^2T_{2g}$ ground-state of $[\text{Fe}(\text{CN})_6]^{3-}$ (eq 1) and to include these together with spin–orbit coupling and magnetic exchange in the χT versus T simulation (*model 2*).

$$H_{\text{LF}}(^2T_{2g}) = \begin{bmatrix} 95 & 120 & -34 \\ 120 & -90 & 118 \\ -34 & 118 & 5 \end{bmatrix} \quad (1)$$

where columns 1, 2, and 3 correspond to $^2T_{2g}(\xi)$, $^2T_{2g}(\eta)$, and $^2T_{2g}(\zeta)$, respectively.

This allowed us to deduce the parameters of the model, that is, the Cu–Fe and Cu–Cu exchange ($J(E)$, $J(B_2)$, and J' , respectively), the Fe^{III} orbital reduction factor k , and the spin–orbit coupling constant ζ (see Figure 3b). There is very good agreement between the values of $J(E)$ and $J(B_2)$ reported here and those calculated by DFT¹¹ (see Table 3). The only worrying result is the exceedingly low value of ζ , deduced from the magnetic data (50.2 cm^{−1} in *trans*-Fe[CuL¹]₂ vs 345 cm^{−1} in $[\text{Fe}(\text{CN})_6]^{3-}$).^{44,45} A possible reason for this unexpected parameter value is the out-of-

phase mixing between the d_{xz} and d_{yz} orbitals of Cu^{II} and Fe^{III}, which leads to a reduction of $\zeta(\text{Fe}^{\text{III}})$ because of contributions with different signs from $\zeta(\text{Cu}^{\text{II}})$.⁴⁶ Alternatively, dynamic Jahn–Teller activity within the $^2T_{2g}$ ground-state of the $[\text{Fe}(\text{CN})_6]^{3-}$ subunit might be responsible for the low value of ζ (Ham reduction).

Model 1 and *model 2* simulate the χT versus T data equally well, but there is a significant difference in the agreement between the experimental and simulated magnetization data. *Model 2* is able to well reproduce the M versus H data and also the isofield lines of the reduced magnetization data (see Figure 3c and Supporting Information, Figure S4, respectively). In contrast, in particular at high field, the values of M are overestimated by the isotropic *model 1* when based on magnetic susceptibility data.

With *model 2*, the ground-state Kramers doublet, dominated by the $M_s = \pm 3/2$ pseudo-spin, is calculated to have a largely anisotropic g -tensor ($g_1 = 0.54$, $g_2 = 0.56$, $g_3 = 5.92$). The less anisotropic g -tensor for the Kramers doublet at 0.14 cm^{−1} higher energy is dominated by $M_s = \pm 1/2$ ($g_1 = 1.94$, $g_2 = 3.38$, $g_3 = 4.72$, see Supporting Information). Ground state spin levels deduced from magnetic data with *model 2* (see Figure 4) have been used for a preliminary interpretation of the temperature-dependent X-band (Figure

(45) Acceptable fits of the χT vs T and magnetization data with slightly larger but still smaller than usual values of ζ are possible (see Supplementary Information, Figures S11–S16) but these do not lead to good enough agreement with the EPR data.

(46) Atanasov, M.; Rauzy, C.; Baettig, P.; Daul, C. A. *Int. J. Quantum Chem.* **2005**, 102, 119.

(44) Atanasov, M.; Comba, P.; Daul, C. A.; Hauser, A. *J. Phys. Chem. (A)* **2007**, 111, 9145.

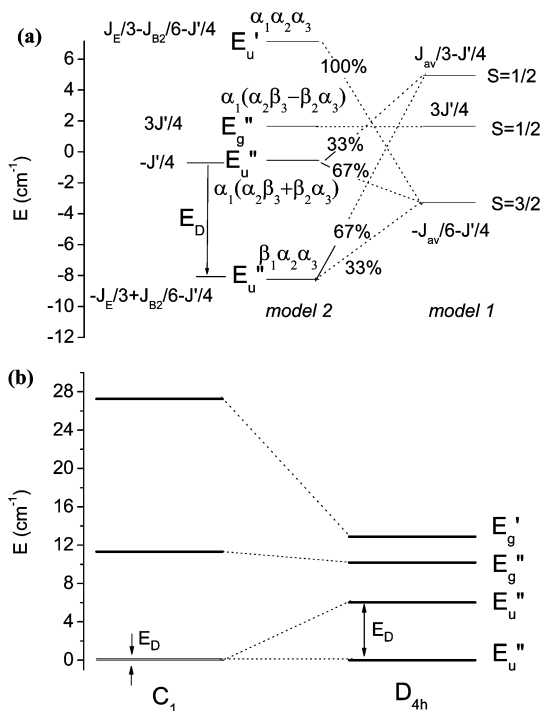


Figure 4. (a) Computed ground-state spin-level diagram for a *trans*-Fe[Cu]₂ model complex with a strictly linear Cu–NC–Fe–CN–Cu axis and an undistorted octahedral [Fe(CN)₆]^{3–} site; left: *model 2*, basis functions, E' ($\alpha_1 = \alpha''$, $\beta_1 = \beta''$) ground-state Kramers doublet of [Fe(CN)₆]^{3–}, E' ($\alpha_{2,3} = \alpha'$, $\beta_{2,3} = \beta'$) Kramers doublets of the two Cu^{II} ions (Cu₂ and Cu₃, see eq S2, S3 in Supporting Information); spin-functions are not normalized and correspond to positive total values of M_s ; spin-functions for negative values of M_s are obtained from those listed upon replacement of α by β and vice versa; right: *model 1*, with an average $J_{av} = J(\text{Cu–Fe})$ value given by $J_{av} = (2J_E + J_{B2})/3$; values of J_E , J_{B2} , and J' are those specified in Figure 3b; (b) Spin levels for *trans*-Fe[Cu]₂ calculated with *model 2* and parameters from Figure 3b with the [Fe(CN)₆]^{3–} site from the X-ray structure (left) and with a regular octahedral [Fe(CN)₆]^{3–} site (right); values of energies (in cm^{–1}): 0.0, 0.14, 11.31, 27.27 (left) and 0.0, 6.02, 10.18, 12.90 (right); g -tensor values (normalized to $M_s = \pm 1/2$) of the two lowest Kramers doublets: $g_1 = 0.54$, $g_2 = 0.56$, $g_3 = 5.92$ ($E = 0.0$), $g_1 = 1.94$, $g_2 = 3.38$, $g_3 = 4.72$ ($E = 0.14$ cm^{–1}; left) and $g_1 = g_2 = 0.43$ (x,y), $g_3 = 6.68$ (z) ($E = 0.0$), $g_1 = g_2 = 1.46$ (x,y), $g_3 = 2.13$ (z) ($E = 6.02$ cm^{–1}; right).

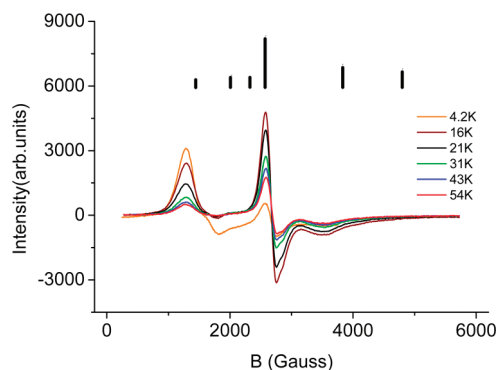


Figure 5. Temperature dependent EPR spectrum at X-band ($\nu = 9.5$ GHz; $T = 4.2$ K, 16 K, 21 K, 31 K, 43 K, 54 K) of *trans*-Fe[Cu]₂ with the calculated magnetic field induction B at resonance conditions and relative intensities of spin-transitions.

5) and also of the W-band EPR spectra (Supporting Information, Figure S2). Resonance magnetic fields (for an X-band frequency of 0.32 cm^{–1}) and intensities of EPR spin transitions (see Supporting Information, Figure S3 for details) allow a qualitative assignment of the observed EPR lines. Upon heating, the depopulation of the lowest Kramers

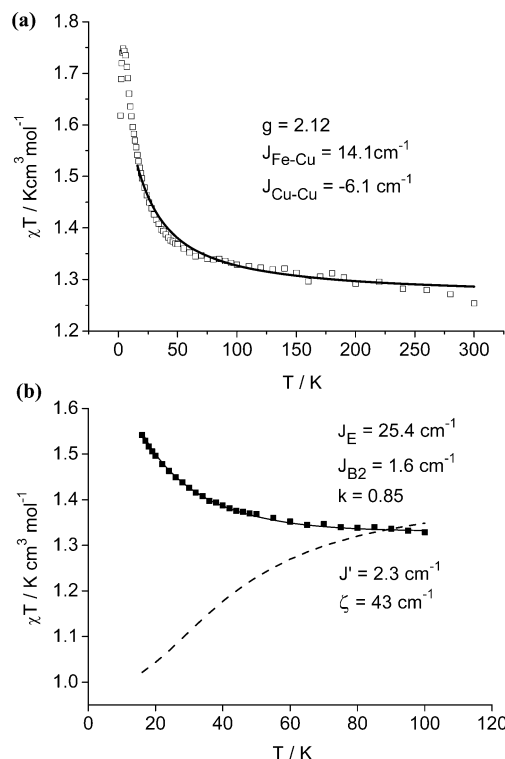


Figure 6. Magnetic properties of *cis*-Fe[Cu]₂. (a) χT vs T diagram (open squares) and best fit using *model 1* with $J(\text{Cu–Fe}) = 14.1$, $J(\text{Cu–Cu}) = -6.1$, and $g = 2.12$. (b) Simulation of the χT vs T data (black squares) with *model 2* [$g(\text{Cu}) = 2.12$]; calculated based on a regular octahedral [Fe(CN)₆]^{3–} site (dashed line).

doublet is accompanied by a decrease in intensity of the low field microwave absorption ($B = 1150$ G in X-band) and by an increase in intensity of the high field EPR absorptions (X-band, 2000 to 4000 G) because of the thermal population of the higher Kramers doublet.

***cis*-Fe[Cu]₂.** Magnetic susceptibility measurements were performed on powdered crystals of *cis*-Fe[Cu]₂ at 1000 G in a temperature range of 2–300 K. The room temperature χT value of 1.254 emu K mol^{–1} is very close to that expected for three uncoupled $S = 1/2$ spins (spin-only: 1.125 emu K mol^{–1}). The χT value increases to a maximum of 1.748 emu K mol^{–1} at a temperature of 3.97 K, which is slightly lower than that expected for an $S = 3/2$ ground state (spin-only 1.875) and clearly manifests a ferromagnetic Fe–Cu coupling (Figure 6). This is further supported by the field dependence of the reduced magnetization (M at 1.8 K, see Supporting Information, Figure S5), which shows saturation ($M = 2.60 \mu_B$), as expected for an $S = 3/2$ ground state. However, this is smaller than the spin-only value ($M = 3.0$) and also reflects orbital contributions, which are more pronounced than for *trans*-Fe[Cu]₂. It was possible to fit the χT versus T data with *model 1* (Figure 6a) but the resulting value of $J = 14.1$ cm^{–1} is unrealistic, that is, much smaller than for *trans*-Fe[Cu]₂. From the experimental structural data of the [Fe(CN)₆]^{3–} site, the matrix of eq 2, which describes the ²T_{2g} sublevels of [Fe(CN)₆]^{3–}, is deduced. A good fit to χT versus T (Figure 6b) and a slightly less satisfactory simulation of the reduced magnetization data (see Supporting Information, Figure S5) allow the model parameters $J(E)$, $J(B_2)$, k ,

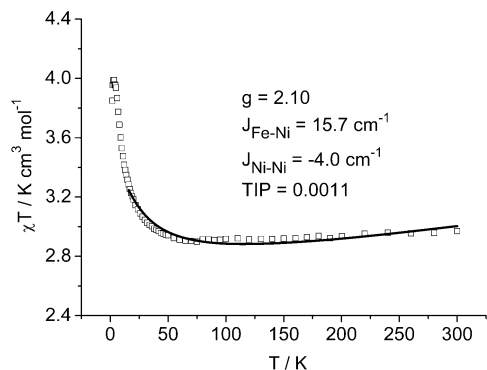


Figure 7. Magnetic properties of *trans*-Fe[NiL¹]₂. χT vs T diagram (black squares) and best fit using *model 1* with $J(\text{Ni-Fe}) = 15.7$, $J(\text{Ni-Ni}) = -4.0 \text{ cm}^{-1}$, and $g = 2.10$ (a TIP correction of 0.0011 has been used).

ζ , and J' to be obtained (Figure 6b). These are similar to those obtained for *trans*-Fe[CuL¹]₂ (see Figure 3b and Table 3).

$$H_{\text{LF}}(^2T_{2g}) = \begin{bmatrix} -167 & 74 & 168 \\ 74 & -368 & -7 \\ 168 & -7 & 535 \end{bmatrix} \quad (2)$$

where columns 1, 2, and 3 correspond to $^2T_{2g}(\xi)$, $^2T_{2g}(\eta)$, and $^2T_{2g}(\zeta)$, respectively.

***trans*-Fe[NiL¹]₂.** Susceptibility measurements of *trans*-Fe[NiL¹]₂ were performed on a powdered sample in an applied field of 500 G and a temperature range of 2 K–300 K (Figure 7). At room temperature the compound exhibits a χT value of 2.970 emu K mol⁻¹, which is higher than expected for two uncoupled Ni^{II} and a *low-spin* Fe^{III} center (spin-only: 2.375 emu K mol⁻¹), and this reflects a considerable orbital contribution to the spin moment. The χT value increases to a maximum of 3.988 emu K mol⁻¹ at a temperature of 3.4 K ($S = 5/2$ spin-only: 4.377 emu K mol⁻¹) and displays a pronounced ferromagnetic Fe–Ni coupling. The low-temperature ($T = 1.8$ K) field dependent magnetization with saturation at $M = 4.684 \mu_B$ supports an $S = 5/2$ ground-state but also shows a negative deviation from the spin-only value of 5. Simulation of the data in terms of the isotropic *model 1* gives a g -value of 2.10 and ferromagnetic $J(\text{Fe-Ni})$, as well as weakly antiferromagnetic $J(\text{Ni-Ni})$ exchange coupling energies (15.7 and -4.0 cm^{-1} , respectively; see Figure 7 and Table 3). However, the value of M at saturation could not be reproduced by *model 1* (Figure 8). Because we have not been able to determine the structure of *trans*-Fe[NiL¹]₂, we could not apply the more elaborate *model 2* and therefore made use of the anisotropic *model 3* to obtain the parameters D , E , and g from a fit to reduced magnetization data (Figure 8). Frequency-domain magnetic resonance spectroscopy measurements (FDMRS) did not show any magnetic resonance absorption lines, which is a further indication for the absence of zero field splitting in the system.

***cis*-Fe[NiL²]₂.** Among the four complexes discussed here in detail, *cis*-Fe[ML²]₂ is that with the largest magnetic anisotropy. Susceptibility measurements were performed on a powdered sample in an applied field of 1000 G and a temperature range of 2 K–300 K (see Figure 9). The room

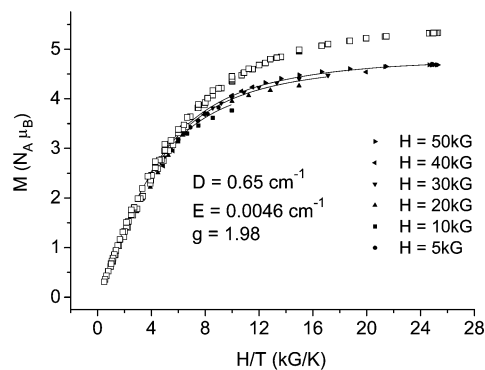


Figure 8. Reduced magnetization data (in units of $N_A \mu_B$; $T = 1.8$ K) of *trans*-Fe[NiL¹]₂; the solid colored lines are simulations with *model 3* ($D = 0.65 \text{ cm}^{-1}$, $E = 0.0046 \text{ cm}^{-1}$, and $g = 1.98$), the open squares are calculated with *model 1*.

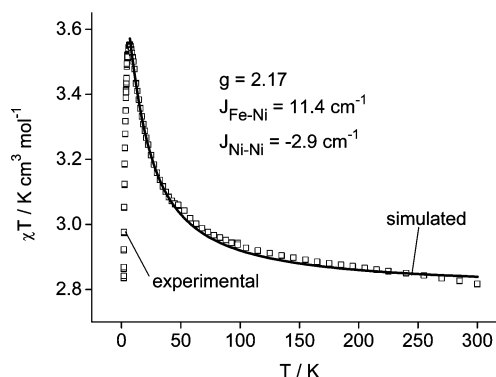


Figure 9. Magnetic data of *cis*-Fe[NiL²]₂. (a) χT vs T diagram (open squares) and best fit using *model 1* (solid line) with $J(\text{Ni-Fe}) = 11.4$, $J(\text{Ni-Ni}) = -2.9 \text{ cm}^{-1}$, and $g = 2.17$.

temperature value of χT is 2.817 emu K mol⁻¹ and is, as that of the *trans* isomer (see Figure 7), higher than expected for two uncoupled Ni^{II} and a *low-spin* Fe^{III} center (spin-only: 2.375 emu K mol⁻¹). This reflects a considerable orbital contribution to the magnetic moment. The χT value increases to a maximum of 3.571 emu K mol⁻¹ at a temperature of 6.0 K ($S = 5/2$, spin-only: 4.377 emu K mol⁻¹) and drops below this temperature, reflecting a significant zero field splitting. On the basis of field-dependent susceptibility measurements in a weak magnetic field, we can exclude any significant intercluster magnetic coupling (see Supporting Information, Figure S8). The Ni–Fe coupling is ferromagnetic, leading to an $S = 5/2$ ground state. This is supported by the low temperature ($T = 1.8$ K) field-dependent magnetization, which saturates at $M = 4.42 \mu_B$ (Supporting Information, Figure S9).

A reasonable simulation of the χT versus T data with *model 1* leads to a ferromagnetic value of $J(\text{Ni-Fe}) = 11.4 \text{ cm}^{-1}$, slightly lower than that of *trans*-Fe[NiL¹]₂, and a weakly antiferromagnetic Ni–Ni exchange coupling energy of $J' = -2.9 \text{ cm}^{-1}$ (see Figure 9). The rather large zero-field splitting parameter $D = 0.91$, derived from *model 3* reflects the pronounced magnetic anisotropy as manifested by the nesting of isofield lines of the reduced magnetizations (Figure 10). No magnetic resonance lines were observed in FDMRS spectra, which could be due to fast spin–lattice relaxation, leading to extremely broad lines. For the sake of comparison we have also performed simulations with *model 3* for the

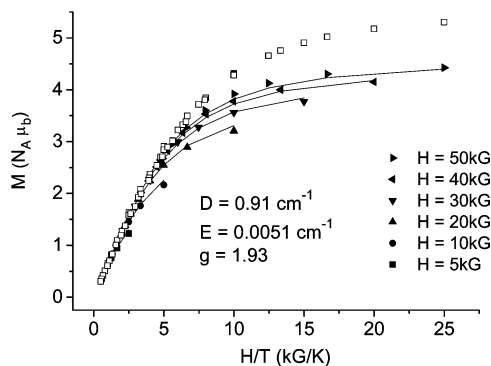


Figure 10. Reduced magnetization data (in units of $N_A \mu_B$; $T = 1.8$ K) of *cis*-Fe[NiL¹]₂; the solid lines are simulations with *model 3* ($D = 0.91$ cm⁻¹, $E = 0.0051$ cm⁻¹, $g = 1.93$), the open squares are calculated with *model 1*.

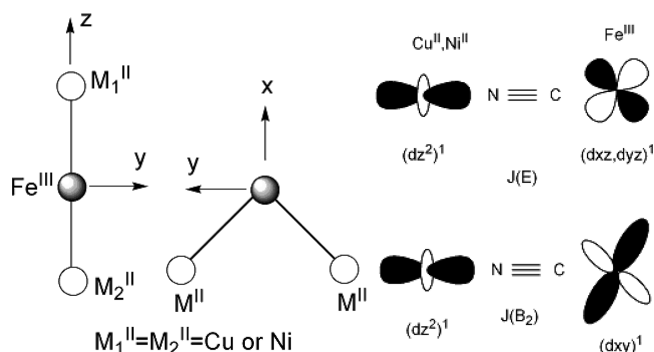


Figure 11. Orientation of the Cartesian axes of the *cis*- and *trans*-Fe[ML]₂ spin clusters and parameters used for the modeling of the M^{II}–Fe^{III} (M = Cu^{II}, Ni^{II}) exchange coupling independence of the orbitally degenerate t_{2g}⁵ electronic configuration of [Fe(CN)₆]³⁻.

Table 4. Fitted D , E , and g values of *cis*- and *trans*-Fe[M]₂

Complex	D	E	g	σ^a
<i>trans</i> -Fe[Cu] ₂	0.44	0.0007	2.12	0.056
<i>cis</i> -Fe[Cu] ₂ ^b	-2.38	-0.014	1.83	0.014
<i>trans</i> -Fe[Ni] ₂	0.65	0.0046	1.98	0.095
<i>cis</i> -Fe[Ni] ₂ ^c	0.91	0.0051	1.93	0.053

^a Standard deviation. ^b An alternative fit with a worse agreement to experiment was also obtained ($\sigma = 0.106$, $D = 2.76$, $E = 0.0006$, and $g = 1.835$). ^c An alternative fit with a worse agreement to experiment ($\sigma = 0.203$, $D = -0.42$, $E = 0.0019$, $g = 1.709$) was also obtained.

trans- and *cis*-Fe[CuL]₂ complexes. Values of D , E , and g are given in Table 4. From the values of D we conclude that the magnetic anisotropy, as quantified by the anisotropy gap energies $2D$ and $4D$ for Fe[Cu]₂ and Fe[Ni]₂, respectively, is larger in the *cis*-Fe[M]₂ compared to the *trans*-Fe[M]₂ complexes.

Discussion

Nature of the Magnetic Exchange Coupling. With the exception of *trans*-Cr[MnL¹]₂, the coupling in the trinuclear M^I[M²]₂ complexes described here is ferromagnetic. With octahedral coordination geometry of each metal ion, unpaired electrons in orbitals of the same symmetry at adjacent coordination centers (t_{2g}–t_{2g}, e_g–e_g) couple antiferromagnetically across the cyanide bridge; those in orthogonal orbitals (t_{2g}–e_g) interact ferromagnetically. Because of the π -overlap between the unpaired electrons in t_{2g} orbitals of Cr^{III} (t_{2g}³) and Mn^{II} (t_{2g}³e_g²), antiferromagnetic coupling is found in

trans-Cr[MnL¹]₂. In *trans*-Fe[MnL¹]₂ the unpaired electron on Fe^{III} (t_{2g}⁵) is also involved in π -overlap with Mn^{II} (t_{2g}³e_g²) and, in contrast to the experimental observation, antiferromagnetic coupling is also expected. The d_{xz} and d_{yz} orbitals of Fe^{III} have the right symmetry for π -overlap with Mn^{II} but are strongly mixed via spin–orbit coupling with the δ -type d_{xy} orbital, and this leads to a weakening of the antiferromagnetic contributions to J . In addition, mixing of the t_{2g} and e_g orbitals of Fe^{III}, because of interaction between the t_{2g}⁵ ground-state and excited-state configurations, introduces antiferromagnetic and a dominating ferromagnetic exchange pathway. As a result, the exchange in *trans*-Fe[MnL¹]₂ is weak and ferromagnetic. A weak ferromagnetic exchange is also found for *trans*-Co[CuL¹]₂. This is supported by DFT calculations and illustrates the effect of the empty e_g orbitals of the closed shell Co^{III} (t_{2g}⁶) center. Cu^{II} and Ni^{II} with one and two singly occupied σ -antibonding e_g orbitals, respectively, and closed shell t_{2g}⁶ configurations provide efficient pathways for ferromagnetic exchange with the π -type ²T_{2g} ground-state of Fe^{III}. The electronic contributions to this exchange coupling have been analyzed in detail.^{10,11} In agreement with the structural data (short and long bonds of Cu to NC and to N-pyridine, respectively) spin density plots of the *cis*- and *trans*-Fe[CuL¹]₂ complexes (see Supporting Information, Figure S1) indicate that the unpaired electron of Cu^{II} is in a d_{x²-y²}-type orbital, with one lobe pointing in the direction of the Cu^{II}–Fe^{III} axis. This results in an efficient σ [Cu(d_{x²-y²)]- π [Fe(d_{xz}d_{yz})]-type magnetic exchange.}

Analysis of the Magnetic Anisotropy—Are SMMs Predictable? For Fe^{III}–M^{II} (M = Cu, Ni) pairs with linear Fe–CN–M bridging geometry and a nondistorted octahedral [Fe(CN)₆]³⁻ site, *model 2* predicts a large magnetic anisotropy with an easy axis of magnetization.¹¹ This arises from the orbital angular momentum $L = 1$ of the ²T_{2g} ground-state of [Fe(CN)₆]³⁻, transmitted by spin–orbit coupling via an orbital-dependent exchange mechanism to the spin ground-state of the magnetic cluster. This mechanism can be extended to a linear M–NC–Fe–CN–M complex (M = Cu^{II}, Ni^{II}) of D_{4h} symmetry with an undistorted [Fe(CN)₆]³⁻ center. An energy level diagram for such a model complex, resulting from the coupling of the ground-state Kramers doublet $E''(\alpha_1 = \alpha'', \beta_1 = \beta'')$ of [Fe(CN)₆]³⁻ with the $S = 1/2$ spin states of two Cu ions, is shown in Figure 4a. The E_u'' ground-state is highly anisotropic ($g_z = 6.68$, $g_{xy} = 0.43$, with the z -axis along the linear Cu–NC–Fe–CN–Cu bridge) and separated by an energy gap E_D from the first excited-state of the same E'' symmetry ($g_z = 0.62$, $g_{xy} = 1.07$). The spin energy gap parameter E_D is analogous to the zero-field splitting parameter D of *model 3* (see eq 10 below). D is usually dominated by contributions from single ions, such as Mn^{III} or Ni^{II} in ligand fields of axial symmetry. In contrast, E_D is dominated by the exchange term J_E which generally is larger than J_{B2} , and this emerges from DFT calculations and experiment (see Table 3).

$$E_D = -\frac{J_E}{3} + \frac{J_{B2}}{6} \quad (3)$$

From a comparison of the calculated value of E_D , derived from regular octahedral geometry of the $[\text{Fe}(\text{CN})_6]^{3-}$ subunit (i.e., setting $H_{\text{LF}}(^2T_{2g}) = 0$, see eq 2, $E_D = -6.0 \text{ cm}^{-1}$; Figure 4b right) and that derived from the observed geometry ($E_D = -0.14 \text{ cm}^{-1}$, Figure 4b left), the anisotropy energy gap E_D is reduced by more than 1 order of magnitude, when the crystallographically determined distortion of the $[\text{Fe}(\text{CN})_6]^{3-}$ site is taken into account. Even small structural changes of $\alpha_{\text{cis}} = 90.00 \pm 1.32^\circ$ (see Table 1) are able to account for the decreased anisotropy. In line with this observation, field dependent reduced magnetization data do not show any significant nesting (Figure 3d).

When we now consider a *cis*- $\text{Fe}[\text{CuL}^2]_2$ model complex with a linear C_{4v} pseudosymmetry of the two $\text{Cu}-\text{NC}-\text{Fe}$ bridges and a $\text{Cu}-\text{Fe}-\text{Cu}$ angle of 90° , we see that this leads to a much lower energy gap parameter ($E_D = -2.0 \text{ cm}^{-1}$). Because of the orientation of the local axes of anisotropy, which are orthogonal to each other within the $\text{Fe}-\text{Cu}_2$ plane, the ground-state is calculated to be less anisotropic ($g_{xy} = 2.93$ in the FeCu_2 plane, $g_z = 2.26$ perpendicular to the FeCu_2 plane). The ligand field splitting of the $^2T_{2g}$ sublevels of the $[\text{Fe}(\text{CN})_6]^{3-}$ site of *cis*- $\text{Fe}[\text{CuL}^2]_2$ has been calculated based on the experimental structural data of the $[\text{Fe}(\text{CN})_6]^{3-}$ site, ($\bar{\alpha}_{\text{cis}} = 90 \pm 2.34$, see Table 1). A larger splitting of the $^2T_{2g}$ term of the $[\text{Fe}(\text{CN})_6]^{3-}$ site is obtained for *cis*- $\text{Fe}[\text{CuL}^2]_2$ ($0.0, 220, 969 \text{ cm}^{-1}$; eq 2) than for *trans*- $\text{Fe}[\text{CuL}^1]_2$ ($0.0, 278, 376 \text{ cm}^{-1}$; eq 1). However, from the splitting pattern of the two complexes it follows that the ground-state of $[\text{Fe}(\text{CN})_6]^{3-}$ in *cis*- $\text{Fe}[\text{CuL}^2]_2$ is much closer to a 2E_g ground-state with orbital contributions which increase the anisotropy.¹¹ Similar to *trans*- $\text{Fe}[\text{CuL}^1]_2$ the parameter E_D in *cis*- $\text{Fe}[\text{CuL}^2]_2$ is very small ($E_D = -0.11 \text{ cm}^{-1}$) but the magnetic anisotropy, reflected by the calculated ground state g -tensor ($g_{xy} = 0.5 \pm 0.1$; $g_z = 5.91$), is appreciable. In contrast to *trans*- $\text{Fe}[\text{CuL}^2]_2$, the low-symmetry distortions in *cis*- $\text{Fe}[\text{CuL}^1]_2$ increase the anisotropy. This is supported by the nesting of the isofield lines of the reduced magnetization (Supporting Information, Figure S5), which is significantly more pronounced (but still small) in *cis*- $\text{Fe}[\text{CuL}^2]_2$ than in *trans*- $\text{Fe}[\text{CuL}^1]_2$.

In addition to the symmetry of the Fe^{III} site (angles α_{cis}), the linearity of the $\text{Fe}-\text{CN}-\text{Cu}$ bridge is expected to affect the anisotropy. While the angles α_{trans} are close to 180° in both complexes, there are significant deviations of the $\text{Cu}-\text{N}-\text{C}$ angles from linearity (averages of the angles γ of 171 and 165.5° for *trans*- $\text{Fe}[\text{CuL}^1]_2$ and *cis*- $\text{Fe}[\text{CuL}^2]_2$, respectively). Because the values of $J(\text{Fe}-\text{Cu})$, computed with *model 2*, are very similar for the two complexes (24.0 and 25.4 cm^{-1} , respectively), we conclude that the nonlinearity of γ does not affect the $\text{Cu}-\text{Fe}$ exchange coupling in the reported range. This also emerges from magneto-structural correlations between J and J' , and the angles α_{trans} and γ , computed by DFT (see Supporting Information, Figure S7).

Finally, we note that in high symmetry, as used for simplicity in Figure 4a, the representation of the spin

energetics in terms of the spin-Hamiltonian defined by *model 3* is not justified because there is strong mixing of states with different values of S . The spin S therefore is not well defined. In the ground-state Kramers doublet E_u'' there is a 2:1 mixing of the $S = 3/2$ and the $S = 1/2$ states. Therefore, we encourage using the new extended Heisenberg Hamiltonian (*model 2*), although it is limited to some extent by a large number of model parameters. However, in combination with spectroscopic methods, which allow to explicitly probe the lowest spin multiplets, such as high-field-multifrequency EPR or inelastic neutron scattering, the model and the emerging parameter values may be further validated.

Conclusions

Pentacoordinate complexes of the divalent metal ions $\text{M}^2 = \text{Mn}^{\text{II}} (S = 5/2)$, $\text{Ni}^{\text{II}} (S = 1)$, and $\text{Cu}^{\text{II}} (S = 1/2)$ with the pentadentate bispidine ligands L^1 and L^2 have been shown to be useful building blocks for the assembly of trinuclear cyanide-bridged complexes based on hexacyanometalates $[\text{M}^1 = \text{Cr}^{\text{III}} (S = 3/2), \text{Fe}^{\text{III}} (S = 1/2), \text{Co}^{\text{III}} (S = 0)]$. In particular, the bispidine ligands have been shown to allow, by subtle structural changes, to selectively stabilize the linear or bent configurations, *trans*- $\text{M}^1[\text{M}^2\text{L}^1]_2$ and *cis*- $\text{M}^1[\text{M}^2\text{L}^2]_2$, respectively. Moreover, the architecture of the bispidine complexes allows, in particular for the Jahn–Teller active Cu^{II} complexes, to stabilize a conformation with an elongation perpendicular to the $\text{M}^1-\text{CN}-\text{M}^2$ axis and a concomitant short M^2-NC bond and maximum magnetic anisotropy.

Magnetic susceptibility and field-dependent magnetization data demonstrate an efficient ferromagnetic exchange coupling which leads to ferromagnetic ground states in the complexes with the $\text{Fe}^{\text{III}}-\text{Cu}^{\text{II}}$ and $\text{Fe}^{\text{III}}-\text{Ni}^{\text{II}}$ exchange-coupled pairs. The analysis of the magnetic data of the *trans*- $\text{Fe}[\text{CuL}^1]_2$ and *cis*- $\text{Fe}[\text{CuL}^2]_2$ spin clusters with an extended Heisenberg model, which accounts for exchange and the multiplet structure due to ligand field effects and spin–orbit coupling of the $[\text{Fe}(\text{CN})_6]^{3-}$ center, leads to the conclusion that the absence of SMM behavior is due to the large angular distortions of the $[\text{Fe}(\text{CN})_6]^{3-}$ central unit and the concomitant quenching of orbital angular momentum of the $\text{Fe}^{\text{III}}(^2T_{2g})$ ground state. However, it is also clear from our model calculations that small distortions due to packing forces and ligand-induced strain may reduce the magnetic anisotropy, and transverse anisotropy due to the off-axial geometry of the bispidine $\text{M}^{\text{II}}\text{L}^1$ and $\text{M}^{\text{II}}\text{L}^2$ building blocks may contribute to a fast relaxation of the magnetization and lead to a loss of SMM behavior.

A careful design of and systematic search for SMMs based on cyanometalates requires an accurate prediction of the molecular and crystal structures. On the basis of earlier developments^{47–56} and our own recent results,^{10,11} it appears

- (47) Palii, A. V.; Tsukerblat, B. S.; Verdager, M. *J. Chem. Phys.* **2002**, *117*, 7896.
- (48) Ostrovsky, S. M.; Werner, R.; Brown, D. A.; Haase, W. *Chem. Phys. Lett.* **2002**, *353*, 290.
- (49) Ostrovsky, S. M.; Falk, K.; Pelikan, J.; Brown, D. A.; Tomkowicz, Z.; Haase, W. *Inorg. Chem.* **2006**, *42*, 2455.
- (50) Palii, A. V.; Tsukerblat, B. S.; Coronado, E.; Clemente-Juan, J. M.; Borrás-Almenar, J. J. *Inorg. Chem.* **2003**, *42*, 2455.

that steric constraints imposed by rigid ligands may be able to impose orbital degeneracy and therefore to systematically increase the magnetic anisotropy in oligonuclear spin clusters.

Experimental Section

Measurements. Infrared spectra (KBr pellets) were recorded with a 16 PC FT-IR (Perkin-Elmer) spectrometer and with a Spectrum 100 FT-IR-Spectrometer (Perkin-Elmer).

UV-vis-NIR spectra were recorded on a V-570 UV/vis/NIR Spectrophotometer (JASCO) as solution in methanol and as diffuse reflection with titanium dioxide or aluminum oxid.

Temperature-dependent EPR spectra were recorded on a Bruker ELEXSYS 500E spectrometer (X-band) as approximately 1×10^{-3} M frozen solution (liquid helium temperatures) in methanol (Supporting Information). Powder X-Band (9.5 GHz) spectra were recorded on a Bruker ESP 300 spectrometer with a rectangular TE₁₀₂ cavity mode. The system is equipped with an Oxford ESR 900 continuous liquid helium flow cryostat for temperature dependent measurements (T is 4.2 to 300 K).

W-band (95 GHz) spectra were recorded on a Bruker Elexsys 680 spectrometer, equipped with a cylindrical resonator which is driven in TE₀₁₁ mode. The magnetic field is produced by a split-coil superconducting magnet which allows applying fields up to 6 T. The system is equipped with an Oxford CF935 continuous helium flow cryostat which allows temperatures between 4.2 K and 320.

Frequency domain magnetic resonance spectroscopy measurements were carried out on a spectrometer that was described before.⁵⁷ The spectrometer utilizes back-ward wave oscillator sources, which are monochromatic and tunable sources. In this technique, the frequency is swept at a fixed applied magnetic field, including zero field. The spectrometer works in the spectral range from 30 GHz up to 1.5 THz and at magnetic fields up to 8 T. A variable temperature insert (VTI) fitted into the cryostat enables us to go to temperatures as low as 1.8 K. All the samples measured were powder pressed pellets of 10 mm diameter and thicknesses between 1 and 3 mm. The powder was mixed with a small amount of eicosane which aids in keeping the pellet together at low temperatures.

Magnetic measurements were carried out either on a MPMS-XL 7T (Quantum Design) SQUID-Magnetometer or on a MPMS-XL 5T (Quantum Design) SQUID-Magnetometer. Samples were powdered and pressed in PTFE tape to avoid field-induced orientation. The data were corrected for diamagnetism of the sample holder and Pascal's constants were used for diamagnetic corrections of the sample.⁵⁸

Elemental analyses were obtained from the microanalytical laboratory of the chemical institutes of the University of Heidelberg.

Syntheses. General Information and Ligands. Chemicals were used as supplied. Technical grade solvents were distilled prior to use. Tetrabutylammonium hexacyanoferrate(III) was prepared as described in literature.⁵⁹ The ligands 3-methyl-9-oxo-2,4-di-(2-pyridyl)-7-(2-pyridylmethyl)-3,7-diazabicyclo[3.3.1]nonane-1,5-dicarboxylic acid dimethyl ester L¹ and 3-methyl-9-oxo-7-(2-pyridylmethyl)-2,4-di-(2-quinolyl)-3,7-diazabicyclo[3.3.1]-nonane-1,5-dicarboxylic acid dimethyl ester L² were obtained as described.^{36–38} **Caution!** Perchlorate salts of metal complexes with organic ligands are potentially explosive. Although we did not experience any problems, such complexes should be handled with care. Cyanide salts are very toxic and should be handled in a well ventilated fume hood.

Bispidine Complexes. The copper(II) complexes of L¹ and L² were produced according to published methods.³⁸ The corresponding nickel(II) and manganese(II) compounds were obtained by addition of a methanol solution of the corresponding metal(II) perchlorate hexahydrate salts (with manganese, the chloride salt was used alternatively) to an equimolar methanol solution of the ligand. With nickel, the resulting purple solution was left in an ether diffusion bath to yield violet crystals. With manganese chloride the solution was refluxed, the solvent removed, and the residue recrystallized from boiling ethanol to give white crystals. With the perchlorate salt only a minimum of MeOH was used, the product solution was heated and then left in a refrigerator (4 °C) for several days.

[Mn(L¹)](ClO₄)₂·2H₂O·MeOH: C₂₉H₃₇Cl₂MnN₅O₁₆ (837.47): calcd C 41.59, H 4.45, N 8.36; found C 41.25, H 4.49, N 8.46.

[Mn(L¹)]Cl₂·1.5H₂O: C₂₈H₃₃Cl₂MnN₅O₇ (677.43): calcd C 49.40, H 4.91, N 10.67; found C 49.05, H 4.95, N 10.23.

[Cu(L¹)](ClO₄)₂·3H₂O: C₂₈H₃₅Cl₂CuN₅O₁₆ (832.05): calcd C 40.42, H 4.24, N 8.42; found C 40.70, H 4.21, N 8.34.

[Ni(L¹)](ClO₄)₂·2H₂O·1MeOH: C₂₉H₃₇Cl₂N₅NiO₁₆ (841.23): calcd C 41.41, H 4.43, N 8.33; found C 41.33, H 4.45, N 8.24.

[Cu(L²)](ClO₄)₂·2H₂O·1MeOH: C₃₇H₄₁Cl₂CuN₅O₁₆ (946.20): calcd C 46.97, H 4.37, N 7.49; found C 46.95, H 4.31, N 7.41.

[Ni(L²)](ClO₄)₂·2H₂O: C₃₆H₃₇Cl₂N₅NiO₁₅ (909.30): calcd C 47.55, H 4.10, N 7.70; found C 47.64, H 4.25, N 7.67.

trans-Fe[CuL¹]₂(ClO₄) (trans-hexa(μ-cyano-1k²N,2k⁶C)-bis[(L¹)-1k⁵N,1k⁵N']copper(II) iron(III) perchlorate hexahydrate). To K₃[Fe(CN)₆] (65.8 mg, 0.2 mmol) in H₂O (2 mL) was added a solution of [Cu(L¹)](ClO₄)₂·3H₂O (325.6 mg, 0.4 mmol) in MeOH:H₂O (1:1, 20 mL). After approximately 5 min green crystals precipitated from the resulting green solution. These were collected on a filter, washed with cold MeOH (5 mL) and Et₂O (5 mL), and then dried in vacuum (yield: 315.3 mg, 0.19 mmol, 99%). C₆₂H₇₀Cl₂Cu₂FeN₁₆O₂₀ (1577.7); calcd C 47.20, H 4.47, N 14.20; found C 47.25, H 4.29, N 14.11. IR (cm⁻¹): 3434 (m, broad), 2952 (s), 2918 (s), 2134 (m), 2106 (m), 1728 (s), 1608 (m), 1572 (w), 1446 (s), 1258 (s), 1108 (s), 769 (s), 623 (s). Electronic spectrum (MeOH): 595 nm; powder (Al₂O₃): 722 nm, 434 nm, 326 nm, 268 nm.

trans-Co[CuL¹]₂(ClO₄) (trans-hexa(μ-cyano-1k²N,2k⁶C)-bis[(L¹)-1k⁵N,1k⁵N']cobalt(III) copper(II) perchlorate tetrahydrate). To K₃[Co(CN)₆] (64.6 mg, 0.2 mmol) in H₂O (2 mL) was added [Cu(L¹)](ClO₄)₂·3H₂O (325.6 mg, 0.4 mmol) in MeOH:H₂O (1:1, 20 mL). The resulting blue solution was left at ambient temperature for 3 days. Slow evaporation led to blue crystals, which were collected on a filter, washed with Et₂O (5 mL) and dried in vacuum (yield: 218.1 mg, 0.14 mmol, 70%). C₆₂H₆₂Cl₂Cu₂CoN₁₆O₁₆ (1544.8); calcd C 48.21, H 4.31, N 14.51; found C 48.47, H 4.31, N 14.56. IR (cm⁻¹): 3434 (m, broad), 3070 (m), 2952 (m), 2924

(59) Das, B.; Carlin, R.; Osteryoung, R. A. *Inorg. Chem.* **1989**, 28, 421.

- (51) Palii, A. V.; Ostrovsky, S. M.; Klokishner, S. I.; Tsukerblat, B. S.; Berlinguette, C. P.; Dunbar, K. R.; Galán-Mascarós, J. R. *J. Am. Chem. Soc.* **2004**, 126, 16860.
- (52) Tsukerblat, B. S.; Palii, A. V.; Ostrovsky, S. M.; Kunitsky, S. V.; Klokishner, S. I.; Dunbar, K. R. *J. Chem. Theory Comput.* **2005**, 1, 668.
- (53) Palii, A. V.; Ostrovsky, S. M.; Klokishner, S. I.; Tsukerblat, B.; Dunbar, K. R. *ChemPhysChem* **2006**, 7, 871.
- (54) Ostrovsky, S. M.; Klokishner, S. I.; Palii, A. V.; Dunbar, K. R. *J. Mol. Struct.* **2007**, 383, 138.
- (55) Klokishner, S. I.; Ostrovsky, S. M.; Palii, A. V.; Dunbar, K. R. *J. Mol. Struct.* **2007**, 838, 144.
- (56) Palii, A. V.; Tsukerblat, B. S.; Clemente-Juan, J. M.; Coronado, E. *Inorg. Chem.* **2005**, 44, 3989.
- (57) Slageren, J. v.; Vongtragool, S.; Gorshunov, B. P.; Mukhin, A. A.; Karl, N.; Krzystek, J.; Telsner, J.; Müller, A.; Sangregorio, C.; Gatteschi, D.; Dressel, M. *Phys. Chem. Chem. Phys.* **2003**, 5, 3837.
- (58) Pascal, P.; Pacault, A.; Hoarau, J. C. R. *Seances Acad. Sci.* **1951**, 233, 1078.

(w), 2151 (m), 2128 (m), 2117 (m), 1725 (s), 1608 (m), 1572 (w), 1446 (s), 1255 (s), 1107 (s), 1048 (m), 786 (s), 769 (s), 623 (s). Electronic spectrum (MeOH): 672 nm.

***trans*-Fe[NiL¹]₂(ClO₄) (trans-hexa(μ-cyano-1κ²N,2κ⁶C)-bis(L¹)-1κ⁵N,1κ⁵N')iron(III) nickel(II) perchlorate trihydrate dimethanol).** To (N^tBu)₄[Fe(CN)₆] (2.048 g, 2.14 mmol) in MeOH (10 mL) was added [Ni(L¹)](ClO₄)₂ (3.522 g, 4.28 mmol) in MeOH (30 mL). Slow evaporation at room temperature of the resulting solution yielded a brown powder, which was collected on a filter, washed with Et₂O (5 mL) and dried in vacuum (yield: 1.9715 g, 1.29 mmol, 58%). C₆₄H₇₂ClFeN₁₆Ni₂O₁₉ (1578.4); calcd C 48.71, H 4.60, N 14.20; found C 48.90, H 4.68, N 14.29. IR (cm⁻¹): 3435 (m, broad), 3077 (m), 2948 (m), 2133 (m), 2116 (m), 1731 (s), 1632 (m), 1606 (s), 1574 (w), 1473 (m), 1447 (s), 1256 (s), 1101 (m), 781 (s), 763 (s), 621 (m). Electronic spectrum (MeOH): 426 nm, 294 nm.

***trans*-Fe[MnL¹]₂Cl (trans-hexa(μ-cyano-2κ²N,1κ⁶C)-bis(L¹)-2κ⁵N,2κ⁵N')iron(III) manganese(II)chloride heptahydrate).** To K₃[Fe(CN)₆] (82.3 mg; 0.25 mmol) in MeOH:H₂O (1:1, 10 mL) was added [Mn(L¹)]Cl₂·H₂O·EtOH (1.06 g, 1.5 mmol) in MeOH (10 mL). This yellow suspension was heated to 55 °C for 4.5 days and then filtered. The residue was washed with Et₂O and dried in vacuum (yield: 350.0 mg, 0.23 mmol, 92%). C₆₂H₇₂ClFeMn₂N₁₆O₁₇ (1514.51); calcd C 49.17, H 4.79, N 14.80; found C 49.28, H 4.75, N 14.71. IR (cm⁻¹): 3432 (s, broad), 3081 (s), 2946 (s), 2116 (s), 2066 (m), 1729 (m), 1602 (m), 1572 (w), 1446 (s), 1270 (s), 1164 (s), 1105 (s), 1043 (s), 1018 (s), 772 (s), 642 (s). Electronic spectrum (MeOH): 422 nm; 316 nm powder (TiO₂): 441 nm.

***trans*-Cr[CuL¹]₂(ClO₄) (trans-hexa(μ-cyano-1κ²N,2κ⁶C)-bis(L¹)-1κ⁵N,1κ⁵N')copper(II) chromium(III)perchlorate hexahydrate).** To K₃[Cr(CN)₆] (65.1 mg, 0.2 mmol) in H₂O (3 mL) was added [Cu(L¹)]ClO₄·3H₂O (325.6 mg, 0.4 mmol) in MeOH:H₂O (1:1, 10 mL) and stirred overnight. The resulting blue suspension was filtered, and the residue washed with MeOH and Et₂O, and dried in vacuum (yield: 223.4 mg, 0.14 mmol, 71%). C₆₂H₇₂ClCrCu₂N₁₆O₁₇ (1573.86); calcd C 47.31, H 4.48, N 14.24; found C 47.01, H 4.28, N 14.13. IR (cm⁻¹): 3422 (s), 3070 (w), 2952 (s), 2918 (s), 2162 (m), 2123 (m), 1729 (m), 1607 (m), 1572 (w), 1448 (s), 1260 (s), 1108 (s), 766 (s), 623 (s). Electronic spectrum (MeOH): 605 nm; powder (TiO₂): 1237 nm, 702 nm, 440 nm.

***trans*-Fe[MnL¹]₂ClO₄ (trans-hexa(μ-cyano-2κ²N,1κ⁶C)-bis(L¹)-2κ⁵N,2κ⁵N')iron(III) manganese(II)perchlorate trihydrate).** To K₃[Fe(CN)₆] (65.8 mg, 0.20 mmol) in H₂O (3 mL) was added [Mn(L¹)]ClO₄·H₂O·EtOH (335.0 mg, 0.4 mmol) in MeOH:H₂O (1:1, 20 mL). Brown-yellow crystals started to precipitate after approximately 1 min. These were recrystallized from hot water and dried in vacuum (yield: 350.0 mg, 0.23 mmol, 92%). C₆₂H₆₄ClFeMn₂N₁₆O₁₇ (1506.44); calcd C 49.43, H 4.28, N 14.88; found C 49.37, H 4.35, N 14.82. IR (cm⁻¹): 3422 (s), 2952 (s), 2918 (s), 2106 (m), 1726 (s), 1604 (m), 1443 (s), 1272 (s), 1121 (s), 1015 (s), 7662 (s), 637 (s). Electronic spectrum (MeOH): 260 nm, 422 nm, 310 nm; powder (TiO₂): 443 nm, 409 nm.

***trans*-Cr[MnL¹]₂ClO₄ (trans-hexa(μ-cyano-1κ²N,2κ⁶C)-bis(L¹)-1κ⁵N,1κ⁵N') chromium(III)manganese(II)perchlorate trihydrate).** To K₃[Cr(CN)₆] (65.1 mg, 0.20 mmol) in H₂O (3 mL) was added [Mn(L¹)]ClO₄·H₂O·EtOH (335.0 mg, 0.4 mmol) in MeOH:H₂O (1:1, 15 mL). The yellow crystals which formed after approximately 10 min were collected on a filter, recrystallized from hot water and dried in vacuum (yield: 231.0 mg, 0.15 mmol, 77%). C₆₂H₆₄ClCrMn₂N₁₆O₁₇ (1502.59); calcd C 49.56, H 4.29, N 14.91; found C 49.82, H 4.34, N 14.96. IR (cm⁻¹): 3422 (s), 3075 (w), 2952 (s), 2918 (s), 2128 (m), 1728 (s), 1605 (m), 1575 (m), 1444 (s), 1279 (s), 1101 (s), 769 (s), 640 (s). Electronic spectrum

(MeOH): 260 nm, 310 nm; powder (TiO₂): 257 nm, 425 nm, 1657 nm. The corresponding chloride salt was obtained in a similar reaction with [Mn(L¹)]Cl₂·H₂O·EtOH (yield: 83%). C₆₂H₆₈ClCrMn₂N₁₆O₁₅ (1474.63); calcd C 50.50, H 4.65, N 15.20; found C 50.51, H 4.69, N 15.18. IR (cm⁻¹): 3428 (s), 2952 (s), 2123 (w), 1728 (s), 1604 (s), 1572 (w), 1474 (s), 1445 (s), 1284 (s), 1253 (s), 1155 (m), 1071 (s), 1037 (s), 1015 (s), 769 (s), 640 (s). Electronic spectrum (MeOH): 260 nm, 310 nm; powder (Al₂O₃): 258 nm, 425 nm, 1658 nm.

The corresponding hexafluorophosphate salt was obtained by a similar reaction with [Mn(L¹)]Cl₂·H₂O·EtOH and adding NH₄PF₆ to the reaction mixture. (yield: 8.31%). C₆₃H₆₄F₆CrMn₂N₁₆O₁₂P (1547.97); calcd C 48.88, H 4.17, N 14.48; found C 49.15, H 4.38, N 14.83.

***cis*-Fe[CuL²]₂(ClO₄) (cis-hexa(μ-cyano-1κ²N,2κ⁶C)-bis(L²)-1κ⁵N,1κ⁵N')copper(II) iron(III) perchlorate).** To K₃[Fe(CN)₆] (131.68 mg, 0.4 mmol) in H₂O (2 mL) was added [Cu(L²)](ClO₄)₂·MeOH·2H₂O (756.96 mg, 0.8 mmol) in MeOH:H₂O (2:1, 30 mL). The resulting green mixture was left for slow evaporation. Green crystals were collected by filtration, washed with Et₂O (5 mL), and dried in vacuum (yield: 471.6 mg, 0.26 mmol, 66%). C₇₈H₈₀ClCu₂FeN₁₆Cu₂O₂₁ (1795.95); calcd C 52.16, H 4.49, N 12.48; found C 52.39, H 4.37, N 12.48. IR (cm⁻¹): 3410 (m, broad), 2958 (s), 2149 (m), 2118 (m), 2079 (m), 1726 (s), 1607 (w), 1504 (m), 1432 (m), 1259 (s), 1107 (s), 1075 (s), 785 (m), 757 (m), 623 (s). Electronic spectrum (MeOH): 264 nm, 294 nm, 306 nm, 318 nm, 420 nm; powder (TiO₂): 697 nm, 447 nm.

***cis*-Fe[NiL²]₂(ClO₄) (cis-hexa(μ-cyano-1κ²N,2κ⁶C)-bis(L²)-1κ⁵N,1κ⁵N')iron(III)nickel(II) perchlorate heptahydrate).** To K₃[Fe(CN)₆] (65.8 mg, 0.2 mmol) in H₂O (2 mL) was added [Ni(L²)](ClO₄)₂ (363.72 mg, 0.4 mmol) in MeOH:H₂O (2:1, 20 mL). From the brown mixture a brown powder precipitated immediately. This was collected on a filter, washed with Et₂O (5 mL) and dried in vacuum (yield: 267.0 mg, 0.15 mmol, 75%). C₇₈H₆₇ClFeN₁₆Ni₂O₁₉ (1750.2); calcd C 53.53, H 4.38, N 12.80; found C 53.62, H 4.48, N 12.78. IR (cm⁻¹): 3424 (m, broad), 3068 (w), 2949 (m), 2149 (w), 2114 (m), 1728 (s), 1623 (m), 1598 (m), 1511 (m), 1432 (m), 1287 (s), 1256 (s), 1121 (s), 785 (w), 750 (w).

***cis*-Co[CuL²]₂(ClO₄) (cis-hexa(μ-cyano-1κ²N,2κ⁶C)-bis(L²)-1κ⁵N,1κ⁵N')cobalt(III) copper(II) perchlorate octahydrate).** To K₃[Co(CN)₆] (66.5 mg, 0.2 mmol) in H₂O (2 mL) was added [Cu(L²)](ClO₄)₂ (378.5 mg, 0.4 mmol) in MeOH:H₂O (10:1, 15 mL). The blue solution was refluxed for approximately 1 min and then left to cool. After 1 h blue crystals formed, were collected, washed with Et₂O (5 mL), and dried in vacuum (yield: 307.2 mg, 0.17 mmol, 85%). C₇₈H₈₂ClCoCu₂N₁₆O₂₂ (1817.06); calcd C 51.56, H 4.55, N 12.33; found C 51.53, H 4.58, N 12.17. IR (cm⁻¹): 3428 (m, broad), 2953 (m), 2923 (m), 2848 (m), 2101 (m), 2021 (m), 1728 (s), 1603 (m), 1445 (s), 1274 (s), 1121 (s), 1015 (m), 783 (m), 768 (m), 757 (m), 636 (w). Electronic spectrum (MeOH): 264 nm, 294 nm, 306 nm, 318 nm, 656 nm; powder (TiO₂): 443 nm, 690 nm, 1022 nm.

X-ray Crystal Structure Determination. Crystal data and details of the structure determinations are listed in Table 5. Intensity data were collected at low temperature with Bruker AXS Smart 1000 CCD and STOE IPDS 1 diffractometers (Mo Kα radiation, graphite monochromator, *I* = 0.71073 Å). Data were corrected for Lorentz, polarization, and absorption effects. The structures were solved by the heavy atom method combined with structure expansion by direct methods applied to difference structure fac-

Table 5. Crystal Data and Structure Refinement for the Complexes *trans*-Cr^{III}[Mn^{II}L¹]₂Cl, *trans*-Fe^{III}[Mn^{II}L¹]₂Cl, *trans*-Fe^{III}[Cu^{II}L¹]₂ClO₄, *cis*-Co^{III}[Cu^{II}L²]₂ClO₄, and *cis*-Fe^{III}[Cu^{II}L²]₂ClO₄

	<i>trans</i> -Cr ^{III} [Mn ^{II} L ¹] ₂ Cl	<i>trans</i> -Fe ^{III} [Mn ^{II} L ¹] ₂ Cl	<i>trans</i> -Fe ^{III} [Cu ^{II} L ¹] ₂ ClO ₄	<i>cis</i> -Co ^{III} [Cu ^{II} L ²] ₂ ClO ₄	<i>cis</i> -Fe ^{III} [Cu ^{II} L ²] ₂ ClO ₄
empirical formula	C ₆₂ H ₆₂ ClCrMn ₂ N ₁₆ O ₁₂ • xH ₂ O	C ₆₂ H ₆₂ ClFeMn ₂ N ₁₆ O ₁₂ • xH ₂ O	C ₆₂ H ₆₂ ClCu ₂ FeN ₁₆ O ₁₆ • xH ₂ O	C ₇₈ H ₇₀ ClCoCu ₂ N ₁₆ O ₁₂ • xH ₂ O	C ₇₈ H ₇₀ ClFeCu ₂ N ₁₆ O ₁₂ • xH ₂ O•CH ₃ OH
formula weight	1385.16	1389.01	1523.67	1644.96	1885.76
temperature /K	100(2)	100(2)	200(2)	150(2)	100(2)
crystal system	triclinic	triclinic	triclinic	triclinic	triclinic
space group	<i>P</i> $\bar{1}$	<i>P</i> $\bar{1}$	<i>P</i> $\bar{1}$	<i>P</i> $\bar{1}$	<i>P</i> $\bar{1}$
unit cell dimensions <i>a</i> /Å	11.250(2)	11.508(1)	11.090(3)	14.302(2)	14.2806(7)
<i>b</i> /Å	12.636(2)	13.576(1)	17.919(3)	15.495(2)	15.5932(8)
<i>c</i> /Å	13.869(2)	14.122(1)	19.387(2)	19.933(2)	19.9964(10)
α /deg	80.350(3)	64.645(3)	75.23(2)	95.388(2)	95.695(1)
β /deg	73.884(3)	73.763(4)	78.89(2)	97.084(2)	96.713(1)
γ /deg	66.791(3)	69.999(4)	84.15(1)	106.062(2)	106.216(1)
volume/Å ³	1737.0(4)	1850.3(3)	3650(1)	4174.3(8)	4205.5(4)
<i>Z</i>	1	1	2	2	2
density (calc.)/ Mg•m ⁻³	1.324	1.247	1.386	1.309	1.489
absorption coefficient/mm ⁻¹	0.580	0.594	0.885	0.800	0.791
<i>F</i> ₀₀₀	716	718	1570	1696	1959
crystal size/mm ³	0.15 × 0.10 × 0.10	0.20 × 0.08 × 0.05	0.3 × 0.25 × 0.15	0.25 × 0.20 × 0.20	0.15 × 0.10 × 0.10
<i>q</i> range for data collection ^o	1.5 to 25.0	1.6 to 23.6	1.8 to 24.0	1.7 to 25.0	1.7 to 25.0
index ranges <i>h</i> , <i>k</i> , <i>l</i> (indep. set)	−12 to 13, −14 to 15, 0 to 16	−11 to 12, −13 to 13, 0 to 15	−12 to 12, −19 to 20, 0 to 22	−17 to 16, −18 to 18, 0 to 23	−16 to 16, −18 to 18, 0 to 23
reflections collected	27827	18496	23442	70061	70391
independent reflections [<i>R</i> _{int}]	6136 [0.0835]	4329 [0.0430]	10760 [0.0796]	14727 [0.0960]	14852 [0.0962]
observed reflections [<i>I</i> > 2σ(<i>I</i>)]	4146	3584	7161	8954	9174
max., min. transmission	0.9623, 0.9260	0.9709 and 0.8905	0.8156, 0.6615	0.8564, 0.8251	0.7461, 0.6209
Data/restraints/ parameters	6136/0/426	4329/3/412	10760/16/905	14727/0/992	14852/3/1153
goodness-of-fit on <i>F</i> ²	1.057	1.111	0.878	0.983	1.063
<i>R</i> indices [<i>F</i> _o > 4σ(<i>F</i> _o)] <i>R</i> (<i>F</i>), <i>wR</i> (<i>F</i> ₂)	0.0584, 0.1507	0.0403, 0.1013	0.0436, 0.1043	0.0577, 0.1435	0.0838, 0.2381
<i>R</i> indices (all data) <i>R</i> (<i>F</i>), <i>wR</i> (<i>F</i> ₂)	0.0851, 0.1621	0.0487, 0.1045	0.0640, 0.1087	0.0917, 0.1573	0.1254, 0.2645
largest diff. peak and hole/e]•Å ⁻³	1.984, −0.603	1.054, −0.359	0.714, −0.538	1.315, −0.696	1.584, −2.053

tors^{60,61} and refined by full matrix least-squares methods based on *F*².^{62,63} All non-hydrogen atoms were given anisotropic displacement parameters. Hydrogen atoms were input at calculated positions and refined with a riding model. All the structures suffered from the presence of variable amounts of water of crystallization and from severe disorder of the anions. To improve the quality of the well-behaved parts of the structures, all except that of *cis*-Fe^{III}[Cu^{II}L²]₂ClO₄ were subjected to the “bypass/squeeze” procedure^{64,65} and the electron density due to the disordered parts was removed from the structures (and the corresponding *F*_{obs}). The presence of linkage isomerism of the bridging cyanides was checked by refinement of the CN/NC-disordered structures. For all complexes, the results indicated absence of linkage isomerism, that is, there was no significant population of the second possible isomer. CIF files giving crystallographic data for the compounds are available from the Cambridge Structural Data Base.

(60) Beurskens, P. T. *Crystallographic Computing 3*; Sheldrick, G. M., Krüger, C., Goddard, R., Eds.; Clarendon Press: Oxford, U.K., 1985; p 216.

(61) Beurskens, P. T.; Beurskens, G.; de Gelder, R.; Smits, J. M. M.; Garcia-Granda, S.; Gould, R. O. *DIRDIF-2007*; Radboud University Nijmegen: Nijmegen, The Netherlands, 2007.

(62) Sheldrick, G. M. *SHELXS-97 Program for structure solution; SHELXL-97 Program for structure refinement*, SHELXS-97; University of Göttingen: Göttingen, Germany, 1997.

Theoretical Background. The geometry and Cartesian axes orientation of the systems considered here are specified in Figure 11. The magnetic data are interpreted with three different model Hamiltonians (*model 1*, *model 2*, and *model 3*). To simulate the χT versus *T* behavior we first apply the broadly used isotropic Heisenberg Hamiltonian of eq 4 (*model 1*) with the two parameters *J* and *J'* to describe the M_{2,3}–Fe^{III} and M₂–M₃' coupling between the *S*_{2,3}–*S*₁ and *S*₂–*S*₃ spins and assuming, as usually done, an isotropic Landé value for the molecular *g*-factor (given by the Zeeman term of eq 4; *model 1*).

$$H_{\text{exc}}^1 = -J\hat{S}_1 \cdot (\hat{S}_2 + \hat{S}_3) - J' \hat{S}_2 \cdot \hat{S}_3 + g\mu_B(\hat{S}_1 + \hat{S}_2 + \hat{S}_3) \cdot \mathbf{B} \quad (4)$$

To account for the orbital degeneracy and spin–orbit coupling within the ²T_{2g} ground-state manifold of [Fe(CN)₆]^{3−} use is made of the extended, orbital-dependent Heisenberg model (*model 2*), described in detail elsewhere.¹¹ Focusing on the trinuclear Fe[CuL]₂ complex it is given by eq 5

(63) Sheldrick, G. M. *Acta Crystallogr.* **2008**, A64.

(64) Sluis, v. d., P.; Spek, A. L. *Acta Crystallogr.* **1990**, A46, 194.

(65) Spek, A. L. *J. Appl. Crystallogr.* **2003**, 36, 7.

$$\hat{H} = \hat{H}_{\text{LF}} + \hat{H}_{\text{SO}} + \hat{H}_{\text{exc}} + \hat{H}_{\text{Z}}(\text{Cu}_2) + \hat{H}_{\text{Z}}(\text{Cu}_3) + \hat{H}_{\text{Z}}(\text{Fe}) \quad (5)$$

To avoid over-parameterization we include all orbital effects on the spin ground-state of Cu^{II} into one effective isotropic value (g) with positive deviations from the spin only value ($g_0 = 2$). We then have $\hat{H}_{\text{Z}}(\text{Cu}_2) + \hat{H}_{\text{Z}}(\text{Cu}_3) = g\mu_B(\hat{\mathbf{S}}_2 + \hat{\mathbf{S}}_3)$ for the Zeeman terms due to Cu_2 and Cu_3 and $\hat{H}_{\text{Z}}(\text{Fe}) = g\mu_B(\hat{\mathbf{S}}_1 + k\hat{\mathbf{L}}_1) \cdot \mathbf{B}$ for the one of $[\text{Fe}(\text{CN})_6]^{3-}$ (k is the covalency reduction factor, $\hat{\mathbf{S}}_1$ and $\hat{\mathbf{L}}_1$ are the spin and orbital moment operators of Fe^{III}). $\hat{H}_{\text{SO}} = \zeta\hat{\mathbf{S}}_1 \cdot \hat{\mathbf{L}}_1$ and \hat{H}_{LF} are the spin-orbit coupling and the ligand field (see below) operators of $[\text{Fe}(\text{CN})_6]^{3-}$ (ζ is the spin-orbit coupling constant of Fe^{III}). Assuming a C_{4v} pseudosymmetry of each $\text{Cu}-\text{Fe}^{\text{III}}$ pair, the orbital dependent exchange term \hat{H}_{exc} of eq 5 can be expressed in terms of the parameters J_E and J_{B2} , defined in Figure 11.

$$H_{\text{exc}} = -\hat{O}_1\hat{\mathbf{S}}_1 \cdot \hat{\mathbf{S}}_2 - \hat{O}_2\hat{\mathbf{S}}_1 \cdot \hat{\mathbf{S}}_3 - J'\hat{\mathbf{S}}_2 \cdot \hat{\mathbf{S}}_3 \quad (6)$$

Within the ξ , η , and ζ electronic basis functions of the parent octahedral $[\text{Fe}(\text{CN})_6]^{3-}$ complex and with the coordinate orientations of Figure 11, the orbital operators \hat{O}_1 and \hat{O}_2 are given by eq 7 (*trans*- $\text{Fe}[\text{ML}]_2$) and eq 8 (*cis*- $\text{Fe}[\text{ML}]_2$).

$$\hat{O}_{1,2} = \begin{bmatrix} J(E) & 0 & 0 \\ 0 & J(E) & 0 \\ 0 & 0 & J(B_2) \end{bmatrix} \quad (7)$$

$$\hat{O}_{1,2} = \begin{bmatrix} \frac{1}{2}[J(E) + J(B_2)] & \pm\frac{1}{2}[J(B_2) - J(E)] & 0 \\ \pm\frac{1}{2}[J(B_2) - J(E)] & \frac{1}{2}[J(E) + J(B_2)] & 0 \\ 0 & 0 & J(E) \end{bmatrix} \quad (8)$$

The Hamiltonian of eq 5 considers the $\text{M}-\text{Fe}^{\text{III}}$ exchange coupling (given by \hat{H}_{exc}) and the multiplet structure (given by $\hat{H}_{\text{LF}} + \hat{H}_{\text{SO}}$) of the $[\text{Fe}(\text{CN})_6]^{3-}$ complex on the same footing; the latter includes a full CI within the basis of the 252 Slater determinants, because of the d^5 electronic configuration of Fe^{III} , and takes low-symmetry ligand field distortions of the $[\text{Fe}(\text{CN})_6]^{3-}$ octahedron, as well as spin-orbit coupling, into account. A procedure has been developed to deduce these multiplet splittings from DFT calculations.^{66–70} A mapping of the full CI problem onto the sublevels, due to the t_{2g}^5 configurations with one hole in the $d_{yz}(\xi)$, $d_{xz}(\eta)$, and $d_{xy}(\zeta)$ orbitals, allows to further reduce the size of the problem to the six microstates which include the $\pm 1/2$ spin of Fe^{III} ⁴⁴ and which are modeled by the ligand field matrix \mathbf{H}_{LF} of eq 9.

$$\mathbf{H}_{\text{LF}} = \begin{bmatrix} V_{\xi\xi} & V_{\xi\eta} & V_{\xi\zeta} \\ V_{\xi\eta} & V_{\eta\eta} & V_{\eta\xi} \\ V_{\xi\zeta} & V_{\eta\xi} & V_{\zeta\zeta} \end{bmatrix} \quad (9)$$

From the six matrix elements of \mathbf{H}_{LF} only five are independent; as the matrix \mathbf{H}_{LF} is traceless we have $V_{\zeta\zeta} = -V_{\xi\xi} - V_{\eta\eta}$. X-ray structural data of *trans*- $\text{Fe}[\text{CuL}]_2$ and *cis*- $\text{Fe}[\text{CuL}]_2$ are used to approximate the matrix \mathbf{H}_{LF} and to refine its matrix elements along with g , k , ζ , J_{B2} , J_E , and J' from a fit to low-temperature magnetic data.

The lack of X-ray structural data for the *trans*- and *cis*- $\text{Fe}[\text{NiL}]_2$ complexes did not allow us to apply *model 2* for these systems. To deduce zero-field splitting parameters and to interpret the low-temperature magnetization data in these complexes use is made of the approximate spin Hamiltonian given by eq 10 (*model 3*).

$$H = D[S_z^2 - S(S+1)/3] + E(S_x^2 - S_y^2) + g\mu_B\mathbf{S} \cdot \mathbf{B} \quad (10)$$

Equation 10 presupposes that the total spin is well defined and only the ground spin state of the molecule is populated. D , E , and g have been treated as adjustable parameters obtained from a fit to low-temperature magnetization data.^{71,72}

Computational Methods. *Models 1, 2, and 3* (see Results, see Theoretical Background) are implemented in a series of programs written in MatLab. These are available from the authors on request.

DFT calculations on the exchange coupling in *trans*- $\text{Fe}[\text{CuL}^1]_2$ and *cis*- $\text{Fe}[\text{CuL}^2]_2$ were done on the geometries observed by X-ray diffraction, using the broken-spin approach. The spin-unprojected formula and the B3LYP functional have been shown to give good results in transition metal exchange coupled pairs^{73–76} and have been used as implemented in the Jaguar program package. Because of the complexity of the electronic structure, the Jaguar code,⁷⁷ which allows a better control of the local spin, multiplicity, and orbital occupations, was chosen to perform the calculations. The Ahlrichs triple ζ basis set with two extra p-polarization functions was used for the transition metal ions and the Ahlrichs double ζ basis was used for all other atoms.^{78,79} The energies of the three Slater determinants $E(\alpha_1\alpha_3\alpha_2)$, $E(\alpha_1\beta_3\alpha_2)$, and $E(\alpha_1\alpha_3\beta_2)$ have been used to calculate $J(\text{Fe}-\text{Cu})$ and $J'(\text{Cu}-\text{Cu})$ according to eq 11.

$$J = \frac{1}{2}[E(\alpha_1\beta_3\alpha_2) - E(\alpha_1\alpha_3\alpha_2)] \quad (11)$$

$$J' = E(\alpha_1\alpha_3\beta_2) - \frac{1}{2}E(\alpha_1\alpha_3\alpha_2) - \frac{1}{2}E(\alpha_1\beta_3\alpha_2)$$

Acknowledgment. Financial support by the Deutsche Forschungsgemeinschaft and the University of Heidelberg are gratefully acknowledged.

Supporting Information Available: The Supporting Informationfiles include spin density plots of *trans*- $\text{Fe}[\text{CuL}^1]_2$ and *cis*- $\text{Fe}[\text{CuL}^2]_2$; details of the X- and W-band EPR spectra of *trans*- $\text{Fe}[\text{CuL}^1]_2$; details of the fits of the magnetic data of all complexes discussed in this paper; a detailed structural data table; the derivation of the matrix of the Hamiltonian for a linear $\text{Cu}-\text{NC}-\text{Fe}-\text{CN}-\text{Cu}$ complex of D_{4h} symmetry with a regular octahedral $[\text{Fe}(\text{CN})_6]^{3-}$ subunit; alternative fits for the *trans*- $\text{Fe}[\text{CuL}^1]_2$ complexes. This material is available free of charge via the Internet at <http://pubs.acs.org>.

IC800556C

(66) Atanasov, M.; Daul, C. A.; Rauzy, C. *Struct. Bonding (Berlin)* **2004**, 106, 97.

(67) Atanasov, M.; Daul, C. A.; Rauzy, C. *Chem. Phys. Lett.* **2003**, 367, 737.

(68) Atanasov, M.; Daul, C. A.; Güdel, H. U.; Wesolowski, T. A.; Zbiri, M. *Inorg. Chem.* **2005**, 44, 2954.

(69) Daul, C.; Rauzy, C.; Zbiri, M.; Baettig, P.; Bruyndonckx, R.; Baerends, E. J.; Atanasov, M. *Chem. Phys. Lett.* **2004**, 399, 433.

(70) Atanasov, M.; Daul, C. A.; Rohmer, M.-M.; Venkatachalam, T. *Chem. Phys. Lett.* **2006**, 427, 449.

(71) Shores, M. P.; Sokol, J. J.; Long, J. J. *Am. Chem. Soc.* **2002**, 124, 2279.

(72) This algorithm has been implemented in the computer program ANISOFIT and applied with great success. An independent code has been written in our group and found to yield identical results.

(73) Ruiz, E.; Rajaraman, G.; Alvarez, S.; Gillon, B.; Stride, J.; Clerac, R.; Larionova, L.; Decurtins, S. *Angew. Chem., Int. Ed.* **2005**, 117, 2771.

(74) Rajaraman, G.; Christensen, K. E.; Larsen, F. K.; Timco, G. A.; Winpenny, R. E. *P. Chem. Commun.* **2005**, 3053.

(75) Rajaraman, G.; Cano, J.; Brechin, K. E.; McInness, E. J. L. *Chem. Commun.* **2004**, 1476.

(76) Ruiz, E.; Alvarez, S.; Rodriguez-Forteza, A.; Alemany, P.; Pouillon, Y.; Massobrio, C. In *Magnetism: Molecules to Materials*; Wiley-VCH: Weinheim, 2001; Vol. II.

(77) JAGUAR 5.5; Schrödinger Inc.: Portland, OR.

(78) Schäfer, A.; Horn, H.; Ahlrichs, R. *J. Chem. Phys.* **1992**, 97, 2571.

(79) Schäfer, A.; Huber, C.; Ahlrichs, R. *J. Chem. Phys.* **1994**, 100, 5829.